Selecting Features for Markov Modeling: A Case Study on HP35

Daniel Nagel, Sofia Sartore, and Gerhard Stock*

Biomolecular Dynamics, Institute of Physics, Albert-Ludwigs-Universität, 79104 Freiburg, Germany.

E-mail: stock@physik.uni-freiburg.de

arXiv:2303.03814v1 [q-bio.BM] 7 Mar 2023

Abstract

Markov state models represent a popular means to interpret molecular dynamics trajectories in terms of memoryless transitions between metastable conformational states. To provide a mechanistic understanding of the considered biomolecular process, these states should reflect structurally distinct conformations and ensure a timescale separation between fast intrastate and slow interstate dynamics. Adopting the folding of villin headpiece (HP35) as a well-established model problem, here we discuss the selection of suitable input coordinates or 'features', such as backbone dihedral angles and interresidue distances. We show that dihedral angles account accurately for the structure of the native energy basin of HP35, while the unfolded region of the free energy landscape and the folding process are best described by tertiary contacts of the protein. To construct a contact-based model, we consider various ways to define and select contact distances, and introduce a low-pass filtering of the feature trajectory as well as a correlation-based characterization of states. Relying on input data that faithfully account for the mechanistic origin of the studied process, the states of the resulting Markov model are clearly discriminated by the features, describe consistently the hierarchical structure of the free energy landscape, and—as a consequence—correctly reproduce the slow timescales of the process.

1 Introduction

Classical molecular dynamics (MD) simulations facilitate the microscopic study of structure, dynamics and function of biomolecular systems.[1] To obtain a concise interpretation of the ever-growing amount of simulation data, we typically want to construct a coarse-grained model of the considered process, such as a Langevin equation[2–4] or a Markov state model (MSM).[5–9] In particular, MSMs have become popular for many practitioners of MD simulations, as they provide a generally accepted state-of-the-art analysis of the dynamics, promise to predict long-time dynamics from short trajectories, and are straightforward to build using open-source packages such as PyEmma[10] and MSMBuilder.[11] The usual workflow to construct an MSM consists of (i) selection of suitable input coordinates, also called 'features', (ii) dimensionality reduction from the high-dimensional feature space to some low-dimensional space of collective variables, (iii) clustering of these low-dimensional data into metastable conformational states, and (iv) estimation of the transition matrix associated with these states. In principle, all these steps can be optimized by employing a variational principle that states that the MSM producing the slowest timescales represents the best model.[12,13] While this is conceptually similar to the well-known variational principle of quantum mechanics where the exact ground-state wave function produces the lowest energy, in practice the analogy is only in part applicable. In particular, it rests on the assumption that the considered process is sufficiently sampled (to ensure that the MD data are statistically meaningful) and is appropriately described by the chosen input coordinates.

Since 'you get what you put in', it is hard to overstate the importance of identifying suitable and relevant input coordinates for the analysis.[14–16] Due to inevitable mixing of overall and internal motion, Cartesian coordinates are in general not suited for dimensionality reduction.[15,17–19] Internal coordinates such as dihedral angles and interatomic distances, on the other hand, are by definition not plagued by this problem and also represent a natural choice, because the molecular force field is given in terms of internal coordinates. While (ϕ, ψ) backbone dihedral angles have been shown to accurately describe the conformation of secondary structures,[20–23] interresidue distances appear to be well suited to also characterize the overall structure of a protein.[24–26] A drawback of using interresidue distances is that their number scales quadratically with the number of residues. To avoid this overrepresentation, it has been suggested to restrict the analysis on distances reflecting interresidue contacts such as hydrogen bonds, salt bridges, and hydrophobic contacts.[27–29] In this way, we focus on the very interactions that cause the studied conformational transition, and consider the long-distance motions as a consequence of these contact changes.

Irrespective of the type of features, it turns out to be important to first exclude irrelevant motions from the analysis. This may include coordinates that do not change during the functional motion (e.g., stable contacts), coordinates that change randomly (e.g., wildly dangling terminal residues that exhibit large amplitude motion), and coordinates describing slow but non-functional motions (e.g., transitions between right- and left-handed helices, where the latter are hardly populated). Apart from merely corrupting the signal-to-noise ratio, such motion may be deceptive for the subsequent dimensionality reduction. For example, principal component analysis maximizes the variance of the first principal components,[30] and is therefore deceived by irrelevant large-amplitude motion. Time-lagged independent component analysis[31] (and other timescale optimizing approaches[12,13]) aims at maximizing the timescales of the first components and is therefore deceived by functionally irrelevant slow motion (such as left to right-handed transitions).[14] To discriminate collective motions underlying functional dynamics from uncorrelated motion, we recently proposed a correlation analysis termed MoSAIC,[32] which

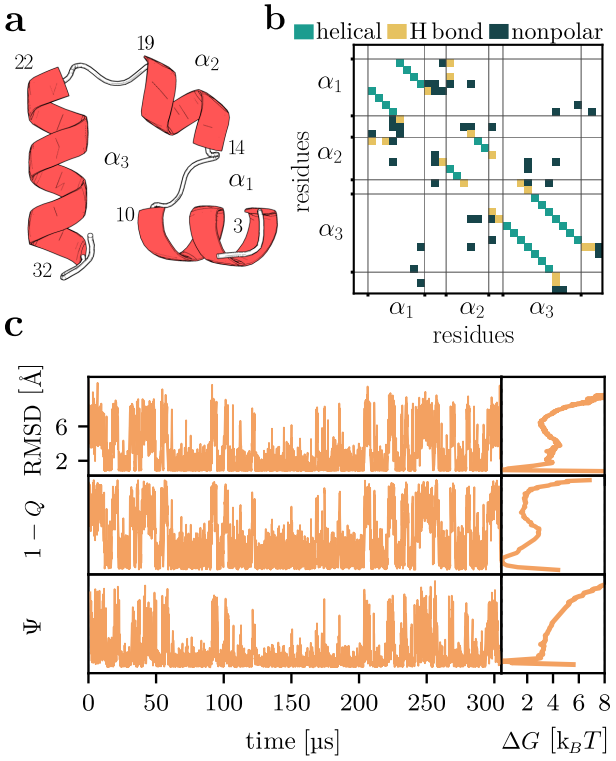

Figure 1: The folding of villin headpiece (HP35). (a) Molecular structure, consisting of three α-helices (residues 3–10, 14–19 and 22–32) that are connected by two loops. (b) Contact map showing the 42 native contacts of HP35. (c) Time evolution of the RMSD (with respect to the C_α-atoms of residues 3 to 33), compared to $1-Q$ (with Q being the fraction of native contacts) and Ψ representing the sum over the backbone dihedral angles ψ_i of the three α-helices. The right side shows the corresponding free energy curves (in units of k_BT) along these coordinates.

block-diagonalizes the correlation matrix of the considered coordinates.

In this work we present a detailed study on the virtues and shortcomings of using contact distances or backbone dihedral angles, for short 'contacts' and 'dihedrals'. As both sets of coordinates appear to describe the protein structure reasonably well, and since metastable molecular structures are thought to represent a physical property of the system, one would assume that this choice of coordinates should not significantly affect the outcome of Markov modeling. On the other hand, because dihedrals and contacts reflect different aspects of the structural dynamics and due to limited sampling, they may result in different collective variables and metastable states, leading to MSMs with different timescales and pathways.

Since such a study depends significantly on the considered system and the specific MD data, here we focus on a well-established model problem, that is, the folding of villin headpiece (HP35),[33–48] see Fig. 1a. In particular, we employ a 300 µs-long MD trajectory of HP35 produced by Piana et al.,[43] which is publicly available from D. E. Shaw Research. Showing the time evolution of the root-mean-square deviation (RMSD) of the MD trajectory from the crystal structure, Fig. 1c reveals that the system undergoes reversible folding and unfolding on a microsecond timescale, which compares well to experimental data.[33–37] A comparison to the fraction of native contacts Q as well as to the sum Ψ over the backbone dihedral angles ψ_i of the three α-helices reveals that both contacts and dihedrals appear to monitor the overall structural evolution of HP35.

The paper starts with a detailed discussion of the choice of suitable features for the folding of HP35. In particular, we consider various ways to define and select contact distances, and introduce a correlation-based characterization of states in terms of contact clusters. Following the description of our workflow to construct the MSM, we discuss the structural and dynamical properties of the metastable conformational states obtained for contacts and dihedrals, and illustrate the insights on the folding process gained directly from the features and from the MSM. The simulation data and all intermediate results, including scripts and detailed descriptions can be downloaded from our Github page https://github.com/moldyn/HP35.

2 Feature selection

All analyses done in this work are based on the 300 µs-long MD simulation (1.5×10^6 data points) of the fast folding Lys24Nle/Lys29Nle mutant of HP35 at $T = 360$ K by Piana et al.,[43] using the Amber ff99SB*-ILDN force-field[49–51] and the TIP3P water model.[52]

2.1 Definition of contacts

The definition of interresidue protein contacts includes

- the conditions when a contact is established, e.g., via a distance cutoff,
- the choice of the molecular structures from which contacts are to be identified, e.g., a single crystal-structure or an ensemble of MD structures, and
- the definition of the distance d_{ij} between two residues, e.g., the distance between the C_α-atoms or between the closest heavy atoms of each residue.

Extending previous work,[27] here we assume a contact to be formed if (1) the distance d_{ij} between the closest non-hydrogen atoms of residues i and j is shorter than 4.5 Å, (2) the residues are more than three residues apart, and (3) the contact is populated more than 30 % of the simulation time ($P_{ij} \geq 0.3$), which ensures that we focus on native contacts. Applied to the MD trajectory of HP35 by Piana et al.,[43] this results in total in 42 native contacts, which include 13 helix-stabilizing $(n, n+4)$ contacts, 20 hydrophobic contacts, and 9 hydrogen bonds, see the contact map shown in Fig. 1b.[53]

Let us discuss the justifications and implications of the above choices. To begin with, the distance cutoff $d_c = 4.5$ Å rests on studies of the distance distribution $P(d_{ij})$ of various proteins, whose prominent peak at short d_{ij} clearly indicates a contact.[54,55] In our experience, this definition covers the vast majority of polar and nonpolar contacts.[27,28] Restricting ourselves to residues that are more than three residues apart, we exclude—apart from irrelevant contacts with next and second next residues—$(n, n+3)$ contacts that occur, e.g., in 3_{10}-helices. While these contacts certainly exist in the unfolded ensemble of HP35, they are very short-lived and therefore of little interest.

Discussing protein folding, it is advantageous to focus on native contacts, because they have been shown to largely determine the folding pathways.[56–58] Moreover, it is well established that the fraction of native contacts Q is highly correlated with the RMSD of the folding trajectory (Fig. 1c) and

therefore represents a well-defined one-dimensional reaction coordinate.[58,59] To this end, we request that the contacts occur at least $P_c = 30\,\%$ of the simulation time, which excludes nonnative contacts that are typically infrequent and short-lived. For somewhat smaller population cutoffs we obtain a higher number of still native contacts (e.g., 56 instead of 42 for $P_c = 10\,\%$), while an increasing number of non-native contacts arise only for significantly lower cutoffs (e.g., in total 122 contacts for $P_c = 1\,\%$). We note that the resulting contacts obtained from the MD trajectory are a different choice of native contacts than the one determined from the crystal structure[35] (PDB 2f4k). The latter exhibits contacts of the N-terminus due to the packing in the crystal, which do not occur in solution (and therefore also not in the MD trajectory). Moreover, these spurious contacts impede the formation of true native contacts such as Asp3-Thr13 and Asp5-Arg14, which turn out important to discriminate various co-existing folded states. See Table S1 for a list of all native contacts found in the crystal structure and the MD simulation.

Apart from the choice of contacts, the appropriate calculation of the contact distance d_{ij} along the trajectory is crucial for the subsequent modeling. While this is straightforward if the contacted atoms roughly remain the same throughout the simulation, it becomes more involved when we consider multicenter contacts between hydrophobic residues involving many and rapidly changing atom pairs. Employing C_α-distances, this problem may be circumvented, however, at the cost of neglecting most microscopic details of the making and breaking of contacts, which typically leads to structurally not well-defined conformational states.[27] Alternatively, we may consider the distance d_{ij} between the closest non-hydrogen atoms of residues i and j, defined by[27]

$$d_{ij}(t) = \min_{n,m} |\boldsymbol{r}_{i,n}(t) - \boldsymbol{r}_{j,m}(t)|, \tag{1}$$

where the indices n and m run over all heavy atoms of the selected residue pair (i, j). Listing population probabilities P_{ij} and life times of all native contacts, Table S1 reveals that this definition of minimum distances leads to somewhat shorter life times but significantly higher populations than those found when only a single atom pair for each contact is used.

When we consider hydrophobic residues with extended and flexible side chains (e.g., Phe, Lys, Met and Nle), however, we find that a large number (say, tens) of connecting atom pairs may occur. In particular, this is the case for protein folding, where during the formation of the hydrophobic core many unusual atom combinations with distances below the cutoff d_c may exist for some short time. Hence, by using the definition in Eq. (1) along the trajectory, we instantaneously choose the atom pair with the minimal distance, regardless how exotic and short-lived this contact might be. Resulting in frequent hopping between multiple atom pairs, this renders the contact definition somewhat ill-defined, because significantly different side-chain conformations may result in a similar contact distance. Hence, when calculating shortest distances between residues, we propose to exclude atom pairs (n, m) that do not meet the population cutoff $P_{nm} \geq 0.3$. This leads to a new definition of minimum distances

$$d_{ij}(t) = \min_{\substack{n,m \\ P_{nm} \geq 0.3}} |\boldsymbol{r}_{i,n}(t) - \boldsymbol{r}_{j,m}(t)|, \tag{2}$$

which will be used throughout this work. As expected, the new criterion significantly reduces the number of considered atom pairs, that is, typically only 2-6 (out of tens) survive. Moreover, the population probability P_{ij} of most contacts is reduced (Table S1), such that 8 (out of 50) of the weaker contacts fall below the overall population cutoff $P_{ij} \geq 0.3$, and are therefore not considered as contacts anymore. (Since redundant contacts between neighboring residues exist, no information is lost.) On the other hand, we obtain considerably longer life times of the contacts, which leads to conformational states of higher metastability.

2.2 Correlation analysis of contacts

To characterize the above defined contacts and detect their interdependencies, it is instructive to calculate the linear correlation matrix

$$\rho_{ij,kl}(t) = \frac{\langle \delta d_{ij} \delta d_{kl} \rangle}{\sigma_{ij} \sigma_{kl}}, \tag{3}$$

where $\delta d_{ij} = d_{ij} - \langle d_{ij} \rangle$ and σ_{ij} is the standard deviation of d_{ij}. (For scalar variables, nonlinear correlation measures typically do not provide essential new information.[32,60]) Since the ordering of the contacts is *per se* arbitrary, we block-diagonalize ρ in order to associate the resulting blocks or clusters with functional motions. Following Diez et al.,[32] this is achieved via a community detection technique called Leiden clustering,[61] using the constant Potts model as objective function and a Leiden resolution parameter $\gamma = 0.78$. All results reported below were produced using the Python package MoSAIC.[32]

Figure 2a shows the modulus of the resulting block-diagonal correlation matrix $\{|\rho_{ij,kl}|\}$, which reveals seven main clusters. Within such a cluster, the contacts are highly correlated (i.e., on average $|\rho_{ij,kl}| \geq \gamma$), while the correlation between different clusters is comparatively low (i.e., $|\rho_{ij,kl}| < \gamma$). As illustrated in Fig. S1 for the first few folding events, high intracluster correlation means that the contacts of a cluster typically change together, i.e., in a cooperative manner. Moreover, there are contacts (or mini-clusters with < 3 contacts) that are not a member of a main cluster but still exhibit moderate correlation with some of the main clusters; they are collected in cluster 8.

To illustrate the contacts contained in the main clusters, Fig. 2b displays the corresponding contact distances inserted into the structure of HP35. We notice that the contact clusters follow nicely the protein backbone from the N- to the C-terminus, such that each cluster features contacts that are located in the same region. In this way, the clusters can be employed to characterize the structure of the various conformational states of the protein, see Fig. 5 below. On the other hand, cluster 8 is found to mostly represent helix-stabilizing contacts along the protein backbone. Interestingly, we find that lifetimes of these helical contacts are typically shorter ($\sim 100\,\mathrm{ns}$) than the contacts of the main clusters ($\sim 1\,\mu\mathrm{s}$), see Tab. S1. As discussed by Buchenberg et al.,[62] this timescale separation indicates hierarchical dynamics, where the fast opening and closing of helix-stabilizing contacts is a prerequisite of overall conformational change to occur.

Since we consider well-populated native contacts and because we study protein folding (which involves the making and breaking of virtually all contacts), there are no coordinates that correlate only weakly with few other coordinates. (This would be the case, e.g., for overall stable contacts and contacts that form and break frequently, which are excluded here.) This is in contrast to the study of functional mo-

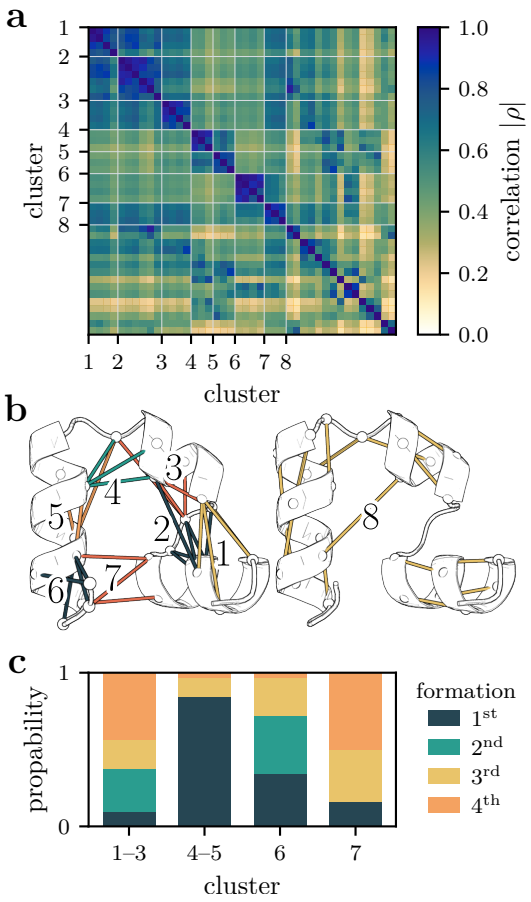

Figure 2: (a) Block-diagonalized correlation matrix of contact distances, revealing seven main clusters and various mini-clusters comprised in cluster 8. Contacts of main clusters are 1: $d_{3,14}$, $d_{3,13}$, $d_{6,14}$, $d_{5,14}$; 2: $d_{7,12}$, $d_{7,13}$, $d_{6,12}$, $d_{7,11}$, $d_{6,11}$, $d_{6,17}$; 3: $d_{12,17}$, $d_{12,16}$, $d_{12,20}$, $d_{13,17}$; 4: $d_{18,25}$, $d_{17,25}$, $d_{20,25}$; 5: $d_{24,28}$, $d_{20,28}$, $d_{25,29}$; 6: $d_{29,35}$, $d_{29,34}$, $d_{30,35}$, $d_{29,33}$; 7: $d_{10,34}$, $d_{9,32}$, $d_{10,29}$; (b) Structural illustration of the interresidue contacts of clusters. (c) Order of clusters formed during a folding event.

tion in a folded protein, where 60–90 % of all contacts were found to be only weakly correlated and could be therefore discarded in the further analysis.[63,64]

2.3 Selection of dihedral angles

Various authors have employed (ϕ_i, ψ_i) backbone dihedral angles of residues i to describe the folding of HP35.[44–47] The number of dihedral angles scales linearly with the number of residues and are valuable conformational descriptors that directly indicate whether the protein forms helices, sheets or loops. While dihedral angles are readily obtained from the MD trajectory and do not require a particular definition (as contact distances do), their periodic nature needs to be taken into account in a statistical analysis.[65–67] For example, we may convert all angles ϑ to sine/cosine-transformed coordinates $(x_1 = \cos\vartheta,\ x_2 = \sin\vartheta)$ in order to obtain a linear coordinate space with the usual Euclidean distance as metric,[18,22,65] and perform the statistical analysis in this space. To avoid the inherent doubling of variables $(\vartheta \to x_1, x_2)$ and the nonlinear nature of the transformation, we may alternatively exploit the well-known Ramachandran plot which demonstrates that protein backbone dihedral angles do not cover the full angular space $(-\pi, \pi]$ but are limited to specific

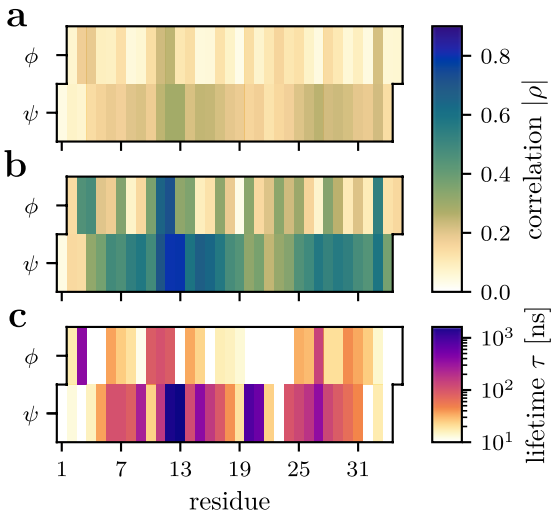

Figure 3: Correlation analysis of (ϕ, ψ) backbone dihedral angles. Shown are (a) the mean correlation of all dihedrals, (b) their correlation with the RMSD shown in Fig. 1, and (c) the decay time of their autocorrelation function. The terminal angles ϕ_1 and ψ_{35} are not properly defined and therefore not shown.

regions due to steric hindrance. Hence, natural cuts between sampled regions can be defined, and by shifting the original data to align the periodic border to this 'maximal gap' in sampling, statistical analyses can be directly performed on the dihedral angles in a standard manner.[66] Combined with a principal component analyses, this approach was termed dPCA+.

When we calculate the correlation matrix of the maximal gap-shifted (ϕ, ψ) dihedral angles, the checkerboard pattern of the matrix indicates that the ψ angles of HP35 are typically much more correlated than the ϕ angles (Fig. S2). Showing the mean correlation (i.e., the average correlation of an angle with all other angles) of all dihedral angles, Fig. 3a confirms this finding. It also shows that the rapidly fluctuating dihedral angles of the first and last two residue hardly correlate with any other angle and therefore should be excluded from the further analysis. (If such uncorrelated motions show transitions between two states, we will get a trivial doubling of states.) Unlike the correlation analysis of contacts, a block-diagonalization of the correlation matrix via Leiden clustering is less instructive (Fig. S2), because backbone dihedral angles naturally proceed with the protein sequence.

Considering the correlation of the dihedral angles with the RMSD of the folding trajectory, Fig. 3b shows that the ψ angles correlate strongly with the folding dynamics of HP35. The finding is in line with the observation that the time evolution of the RMSD and of the sum of the ψ angles are highly correlated (Fig. 1c). This is expected, because ψ angles decrease significantly in the Ramachandran plot when the conformation changes from extended to helical structures, and therefore account directly for the helicity of the system. The importance of the ψ angles is also apparent from the long decay times of their autocorrelation functions shown in Fig. 3c. This suggests that, except for the terminal residues 1–2 and 34–35, we want to include all ψ-angles in the further analysis.

While most ϕ angles change only little when the residue changes from extended to helical structures, there are prominent exceptions to residues in the termini and the two loops.

Apart from the glycines Gly11 and Gly33, in particular the ϕ angle of Asp3 is found to coexist in left- and right-handed conformations, which leads to a splitting of the states in the native energy basin,[27,45,68] see below. These residues reveal also slowly decaying autocorrelation functions, while the majority of the ϕ motions is rather short-lived. Since the helical ϕ-angles contribute only minor to the first PCs, we decided to include all of them (except for the terminal residues) in the further analysis. In total, this results in 62 dihedral angles as features.

3 Construction of metastable states

To identify metastable conformational states from the above defined feature trajectories, the following protocol is used. First we employ a Gaussian low-pass filter that eliminates high-frequent fluctuation of the feature trajectory. We then use principal component analysis[30] (PCA) in order to convert the high-dimensional feature variables to low-dimensional ($\lesssim 5$) collective variables.[69–71] The low dimensionality facilitates robust density-based clustering,[68] which is used to generate (typically hundreds of) microstates. Using the most probable path algorithm[72] (MPP) to lump the microstates into a few macrostates, we obtain the desired set of metastable conformational states. Finally, we use the projection method of Hummer and Szabo,[73] to construct the transition matrix of the metastable states, and provide a detailed characterization of their structural and dynamical properties. All analyses shown in this paper were performed using our open-source Python package msmhelper, which can be downloaded from https://github.com/moldyn. To facilitate the reproduction and analysis of our results, we furthermore provide trajectories of all intermediate steps. Using an Intel Core i9-10900 processor and two NVIDIA GeForce GTX 680, the complete above described MSM workflow (filtering, PCA, clustering) applied to 1.5×10^6 data points required a wall clock time of about 16 min. Moreover, we spent about 2 h on contact definition, 3 min on angle definition, 30 min for the MSM analyses shown in Fig. 7, and in total 9.5 h for the XGBoost analyses shown in Fig. 6.

3.1 Data filtering

While the typical lifetime of the selected contact and dihedral variables of HP35 is between 0.1 and 1 µs (Tab. S1 and Fig. 3c), the variables are found to fluctuate on a picosecond timescale, reflecting fast moving atoms in the vicinity. Since we eventually want to define metastable conformational states from the variables, we face the problem that the resulting state trajectory may also fluctuate rapidly between various states when the contacts are close to the distance cutoff. This is in contrast to the fact that state changes are associated with rare transitions over free energy barriers (cf. Fig. 1c), i.e., they are expected to occur infrequently and without spurious back-transitions. The problem is caused by the projection of the high-dimensional protein dynamics onto low-dimensional variables (i.e., the contact distances or dihedral angles). This may lead to misclassification of the data points in the transition regions,[45] which are notoriously undersampled in unbiased MD simulations.

As a simple but effective remedy, it has been suggested that a transition from one state to another must reach the core region of the other state; otherwise, it is not counted as a transition.[5,74,75] Alternatively, we may request that the trajectory spends a minimum time in the new state for the transition to be counted.[44,45] While this 'dynamic coring' is capable of correcting spurious transitions, it cannot correct a wrong state assignment caused by them. This means, for example, that if two states overlap due to suboptimally chosen collective variables and can therefore no longer be discriminated, the correct state assignment cannot be reconstructed from coring. The same holds for alternative approaches of dynamic correction that are subsequent to clustering.[5,74,75]

As a new approach, we propose to perform the dynamic correction as the first step in the workflow. Here we use a Gaussian low-pass filter to smoothen the high-frequency fluctuations of the feature variables $d(t)$, i.e.,

$$d(t) \to \sum_j g(t,t_j) d(t_j), \tag{4}$$

$$g(t,t_j) = \frac{1}{\sqrt{2\pi\sigma^2}} \exp\left[\frac{-(t_j-t)^2}{2\sigma^2}\right] . \tag{5}$$

Choosing $\sigma = 2$ ns, the Gaussian filtering suppresses all subns fluctuations and makes a subsequent coring of the resulting conformational states obsolete. We will discuss the effects of the filtering ansatz in comparison to dynamic coring at the end of Sec. 3.5.

3.2 Dimensionality reduction

PCA represents a linear transformation that diagonalizes the correlation matrix and thus removes the instantaneous linear correlations among the variables. Ordering the eigenvalues of the resulting eigenvectors decreasingly, the first principal components (PCs, i.e., the projection of the input coordinates on the eigenvectors) account for the directions of the largest correlation of the data set.[30] While PCA becomes exact if sufficiently many PCs are included, we aim to obtain a low-dimensional representation by truncating the number of PCs according to the following criteria: Non-quadratic appearance of the free energy curves along the PCs, decay times of their autocorrelation function, and explained percentage of the total correlation.[20]

Using contact distances, we find that the first 5 PCs exhibit a multimodal structure of their free energy curves, reveal the slowest timescales ($\sim$ 0.1–2 µs), and explain $\sim 80\,\%$ of the total correlation (Fig. S3). The first PC mostly reflects the fraction of native contacts Q (Fig. 1c), which represents a well-established reaction coordinate.[58,59] The higher PCs account for linear combinations of contact changes in various MoSAIC clusters (Fig. 2). Considering dihedral angles, only the first 4 PCs exhibit nontrivial free energy curves. They account for slowest timescales ($\sim$ 0.1–2 µs), and explain $\sim 50\,\%$ of the total correlation (Fig. S3). The first PC represents the sum Ψ of all ψ angles (Fig. 1c), which describes the overall helicity of the protein. The higher PCs mainly account for dihedral angle changes of helix 1 and helix 3.

3.3 Clustering

In a first step, we use robust density-based clustering,[45,68] which computes a local free energy estimate for every frame of the trajectory by counting all other structures inside a hypersphere of fixed radius R. When we then reorder all structures from low to high free energy, the minima of the free energy landscape can be identified. By iteratively increasing an energy threshold, all structures with a free energy below

that threshold that are closer than a certain lumping radius r_l will be assigned to the same cluster, until all clusters meet at their energy barriers. In this way, all data points are assigned to a cluster as one branch of the iteratively created tree. Considering contact distances, we used a hypersphere $R = r_l \approx 0.124$ equaling the lumping radius. For dihedral angles, we choose $R = r_l \approx 0.072$ rad. Figure S4a shows the resulting total number of microstates obtained as a function of the minimal population $P_{\min}$ a state must contain. Here we chose $P_{\min} = 0.01\,\% \mathrel{\widehat{=}} 153$ frames, resulting in 522 and 330 microstates for contact distances and dihedral angles, respectively.

In a second step, we adopt the MPP algorithm [72] to construct a small number of macrostates. Starting with the above defined microstates, MPP first calculates the transition matrix of these states, using a lag time $\tau_{\mathrm{MPP}} = 10$ ns. (The choice of τ_{MPP} is explained in the discussion of Fig. 7a below.) If the self-transition probability of a given state is lower than a certain metastability criterion $Q_{\min} \in (0, 1]$, the state will be lumped with the state to which the transition probability is the highest. This procedure is reiterated, until there are no more transitions for a given $Q_{\min}$. Repeating the procedure for increasing $Q_{\min}$, we construct a dendrogram that shows how the various metastable states merge into energy basins, thus illustrating the topology and the hierarchical structure of the free energy landscape. To facilitate the handling of many states, we use an automatic branch detection scheme. [76]

Figure 4 shows the resulting dendrograms obtained for (a) contacts and (b) dihedral angles. For $Q_{\min} \gtrsim 0.9$, we obtain only two macrostates, as all microstates are assigned either to the native or the unfolded energy basin of HP35. Coloring the states according to their mean number of native contacts, the native states are drawn in purple and the unfolded in yellow to orange. Although the unfolded basin clearly contains more microstates, the native basin is higher populated ($\approx 68\,\%$). By decreasing the requested metastability $Q_{\min}$, we in effect decrease the requested minimum barrier height between separated states, such that the two main basins split up in an increasing number of metastable states. Requesting that a metastable state should have at least $Q_{\min} = 0.5$ and a minimum population of 0.5 % for contacts and 0.1 % for dihedrals, we obtain 12 metastable states for both contacts and dihedral angles. [77] While overall the two dendrograms look similar, we find that dihedrals appear to yield a more structured native basin, while contacts seem to resolve the unfolded basin better. In particular, contacts reveal that the unfolded basin splits up in various well-characterized metastable states, demonstrating that the unfolded basin exhibits nontrivial dynamical structure. Overall, we wish to stress that the MPP dendrogram color-coded with reaction coordinate Q shows clearly whether only structurally similar states are merged, thus providing an insightful test of the quality of the state partitioning.

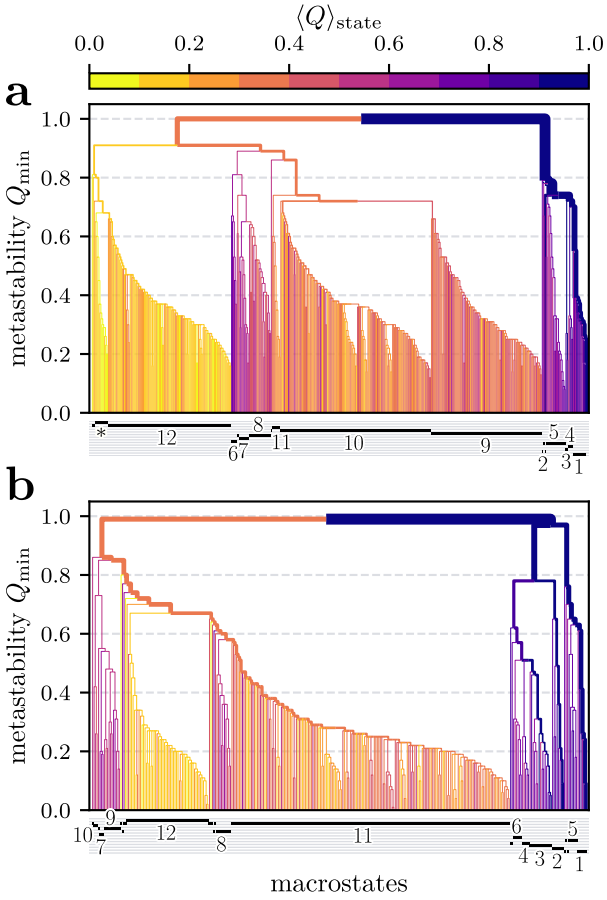

Figure 4: MPP dendrogram illustrating the clustering of microstates into metastable states upon increasing the requested minimum metastability criterion $Q_{\min}$ of a state. Results are shown for (a) contacts and (b) dihedral angles. The states are colored according to their mean number of native contacts $\langle Q \rangle_{\mathrm{state}}$ from yellow (unfolded) via orange to native (purple). Black horizontal bars at the bottom indicate which microstates are contained in a metastable state.

3.4 Structural characterization of states

To obtain a useful state model, the conformational states identified above should be structurally well-defined (to represent distinct conformational ensembles) as well as long-lived or metastable (to give a good MSM). As a structural characterization, Fig. 5 shows the distribution of contact distances for each state, as obtained for (a) contacts and (c) dihedral angles. Similarly, Fig. S4b shows the corresponding dihedral angle distributions for the two cases. Since contact distances exhibit a bimodal distribution (reflecting formed and broken contacts) such that mean and variance do not well describe the data, we use a box-plot representation with quartiles Q_i comprising the first $i \cdot 25\,\%$ of the data. The states are ordered by decreasing fraction of native contacts, such that state 1 is the native state (all contact distances are shorter than $d_c = 4.5$ Å) and state 12 is the completely unfolded state with a broad distribution of large distances. The contacts are ordered according to the seven main MoSAIC clusters defined in Fig. 2, which follow the protein backbone from the N- to the C-terminus.

Interestingly, we find that the MoSAIC clusters provide a concise characterization of the structure of the metastable states. The first three states are structurally well-defined native-like states, which combine 62 % and 64 % of the total population for contacts and dihedrals, respectively. As discussed below, these states differ in details of helix 1. According to the MPP dendrogram (Fig. 4), states 4 and 5 (for contacts) and states 4 to 6 (for dihedrals) also belong to the native energy basin. Compared to state 1, they are characterized by broken contacts on the C-terminal side. The unfolded basin mainly consist of states 9 to 12, which show different degrees of disorder. For contacts, hardly any contacts exist in state 12, while states 9 and 10 at least exhibit formed contacts in clusters 4 and 5, and (for state 9) in clus-

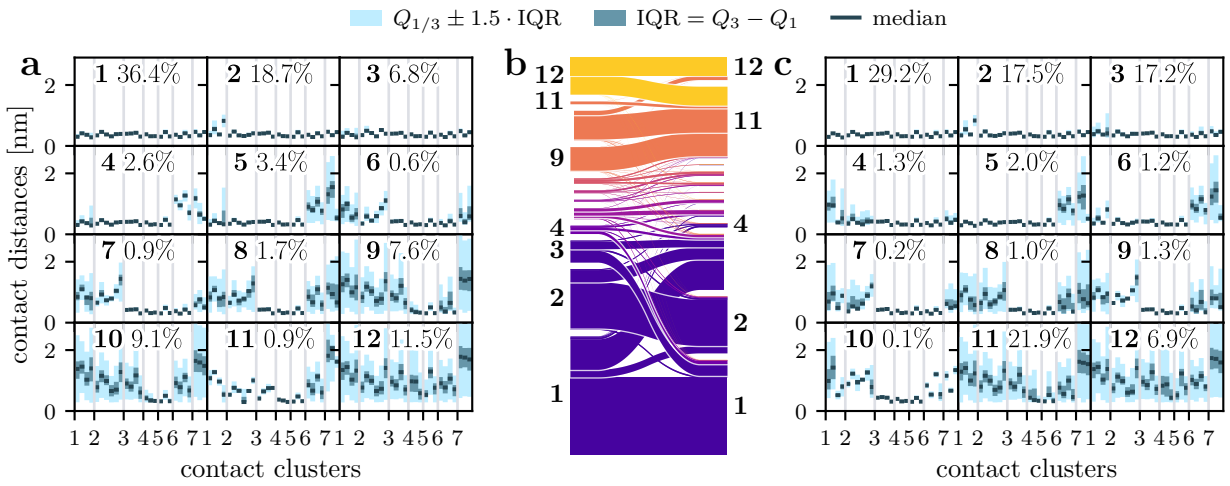

Figure 5: Structural characterization of the twelve metastable states of HP35, obtained for (a) contacts and (c) dihedral angles. The states are ordered by decreasing fraction of native contacts Q, the contacts are ordered according to the seven main MoSAIC clusters (Fig. 2). For each state, the distribution of contact distances are represented by the median Q_2, the interquartile range $\mathrm{IQR} = Q_3 - Q_1$ and the lower (upper) bound as the smallest (largest) data point in $Q_{1/3} \pm 1.5 \cdot \mathrm{IQR}$. (b) Sankey diagram depicting the relation between the two state definitions. The color code (see Fig. 4) reflects the fraction of native contacts Q.

ter 6. For dihedrals, this splitting of the unfolded states in different structures is less obvious. Finally, there are several lowly populated ($\lesssim 1\,\%$) intermediate states to be discussed below.

The state partitions obtained for contacts and dihedrals can be directly compared in a Sankey plot (Fig. 5b). We find a simple correspondence between the main three native states, as well as between the main two or three unfolded states. However, there is no such clear relation for the lowly populated in-between states, which are assigned differently for contacts and dihedrals. To summarize, by focusing on the (clustered) features that describe the considered process, the contact representation provides a concise but sufficient structural characterization of the metastable states.

As a further state characterization, we consider the essential coordinates of the system, i.e., the most important features to discriminate the metastable states. To this end, we employ a recently proposed machine learning approach [78] that uses the decision tree-based program XGBoost, [79] which trains a model to assign MD structures to the state they most probably belong to. By determining the feature importance for the state definitions, the algorithm iteratively eliminates the least important coordinate from the training set. Proceeding this way, Fig. 6 shows that 6 contacts or 10 dihedrals are sufficient to discriminate all metastable states with high accuracy. Somewhat surprisingly, the most important contacts are between residue pairs $(3, 13)$, $(6, 17)$ and $(5, 9)$ involving helix 1, because they define the three highly populated states of the native basin. The main unfolded states are characterized by tertiary contact $(20, 28)$, which holds helix 2 and helix 3 together. The lowly-populated intermediate states moreover require mainly contacts $(6, 10)$ and $(9, 32)$ for their identification. The situation is somewhat different for dihedral angles, where the most important coordinate is ϕ_3, which is sufficient to discriminate the three main native states (see Fig. S4c). With the exception of the second most unfolded state 11 whose definition mainly requires ψ_{12}, the discrimination of intermediate and unfolded states requires multiple dihedral angles located in all three helices. Hence, we have learned that the substates of the native basin are best described by dihedral angles;

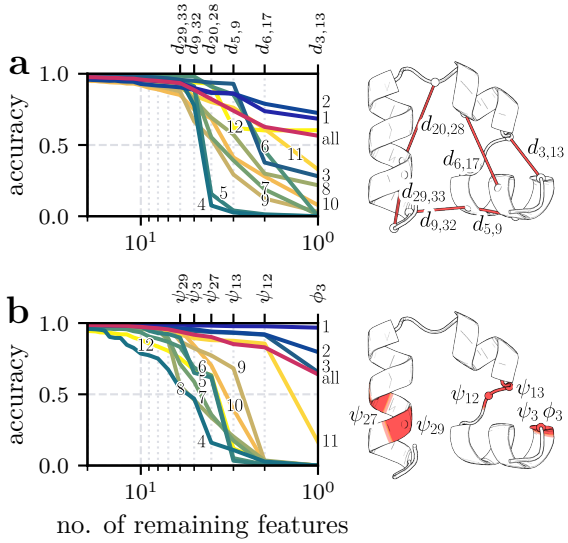

Figure 6: Identification of essential coordinates by decision tree-based machine learning, [78] obtained for (a) contacts and (b) dihedral angles. Shown is the accuracy loss of the model when we discard in every step the least important feature. Employing XGBoost, [79] we used a learning rate $\eta = 0.7$, a tree depth of 8, and 50 training rounds in every step.

in fact a single angle, ϕ_3, suffices for HP35. On the other hand, the overall folding of the protein and the substates of the unfolded basin are best described by tertiary contacts connecting the helices.

3.5 Dynamical properties of states

To assess the dynamical properties of our states, we calculate the transition matrix T_{ij}, describing the probability of a transition between states i and j during some chosen lag time τ_{lag}. By diagonalizing the transition matrix, we obtain its eigenvalues λ_n and the implied timescales $t_n = -\tau_{\mathrm{lag}} / \ln \lambda_n$. For Markovian dynamics these timescales should be constant [cf. Eq. (6)]; since that is usually not the case for

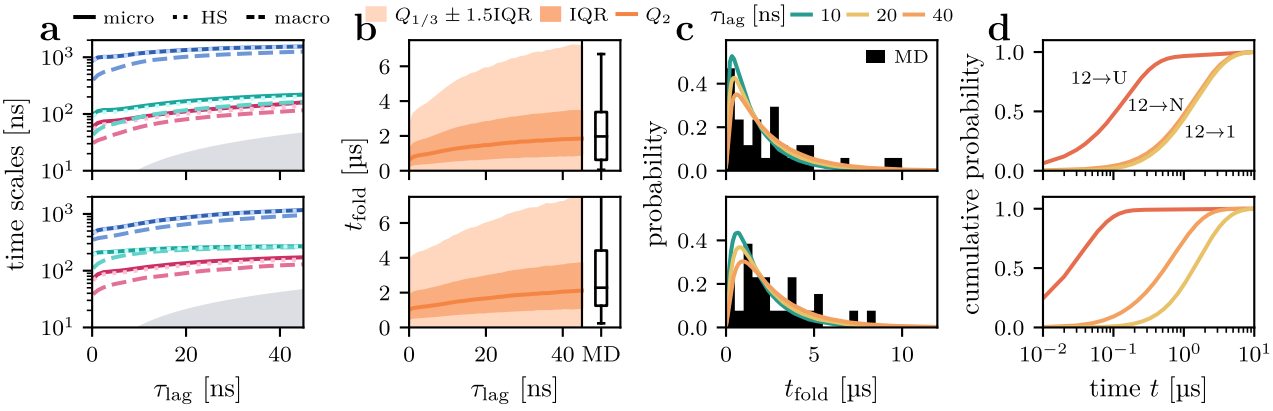

Figure 7: Timescales and folding dynamics exhibited by MSMs constructed from contacts (top) and dihedrals (bottom). (a) First three implied timescales t_n shown as a function of the lag time τ_{lag}, obtained for the microstates (full lines) and for the macrostates, either assuming local equilibration (dashed lines) or using the projection method of Hummer and Szabo [73] (thin lines). Gray areas indicate that $t_n \leq \tau_{\mathrm{lag}}$. (b) Box-plot representation of the folding time distributions obtained from MSMs and MD data. (c) Histogram of the MD folding times t_{fold} from state 12 to state 1, compared to MSM folding time distributions for various lag times. (d) Time evolution of various cumulative population probabilities, obtained for $\tau_{\mathrm{lag}} = 10$ ns. Starting in the completely unfolded state 12, the probabilities $P_{12\to\mathrm{U}}(t)$ reflects the hydrophobic collapse of the protein to the other states of the unfolded basin, $P_{12\to\mathrm{N}}(t)$ accounts for the time that the system remains in the unfolded basin, and $P_{12\to1}(t)$ describes the overall folding process into the native state 1.

short lag times, constancy of implied timescales can be used as a criterion to choose a suitable τ_{lag}.[7] Figure 7a shows the resulting implied timescales t_1–t_3 reflecting the three slowest processes. We first consider the timescales of the microstates, which are generally found to level off for lag times $\tau_{\mathrm{lag}} \gtrsim 10$ ns for contacts and dihedrals. As anticipated above, this value of τ_{lag} is used for MPP clustering to define macrostates.

Considering the macrostates, various methods exist to calculate the corresponding transition matrix. Assuming local equilibration within the macrostates, it can be directly computed from the associated count matrix (as done for the microstates). Alternatively, we may invoke an approach to optimally project the microstate dynamics onto the macrostate dynamics,[80–83] as achieved by the method of Hummer and Szabo.[73] Since the direct calculation yields on average 40 % shorter timescales while the latter virtually reproduces the timescales of the microstates (Fig. 7a), we generally employ the projection method in the following. Similarly, as found for the microstates, the implied timescales of the macrostates level off for lag times $\tau_{\mathrm{lag}} \gtrsim 10$ ns. Hence, if not noted otherwise, all further discussion will be based on this value. For further reference, Tab. S2 lists the interstate transition times and state lifetimes associated with the resulting transition matrices for contacts and dihedrals.

The resulting macrostate timescales obtained for contacts and dihedrals are compared in Fig. 7a. In the case of contacts, the slowest timescale of about 1.2 µs is clearly separated from the next ones ($\sim$ 0.10 and 0.08 µs). Inspecting the eigenvectors of the transition matrix (Fig. S5a), we find that the slowest process corresponds to the transition from unfolded states (12, 10 and 9) to folded states (1, 2 and 3), while the second slowest process describes transitions from the completely unfolded state 12 to partially unfolded states 6–10. For dihedrals, the slowest timescale is significantly lower ($\sim$ 0.7 µs), followed by two clearly separated timescales ($\sim$ 0.2 and 0.1 µs). The slowest process corresponds again to the transition from unfolded (12, 11) to folded states (1, 2 and 3), while the second eigenvector mostly accounts for transitions from state 1 to state 2 and 3 in the native basin. The significantly longer first implied timescale found for contacts (1.2 µs) compared to dihedrals (0.7 µs) is a consequence of the more apparent timescale separation exhibited by the corresponding first PCs (Fig. S3).

To see how the implied timescales translate to measurable observables of the folding process, we next consider the distribution of the folding time t_{fold}, defined as the waiting time for the transition of the completely unfolded state 12 to the native state 1. To this end, we employed 10^9 steps of a Markov chain Monte Carlo propagation, where a trajectory is sampled from the given transition matrix by drawing random numbers which determine the next step. Shown in Fig. 7b as a function of the lag time τ_{lag}, the resulting folding time is found to increase only little with τ_{lag}. While the median of the MSM prediction of t_{fold} somewhat underestimates the MD result, overall the MSM reproduces the rather broad MD folding-time distributions for both contacts and dihedrals quite well. (We note in passing that, despite the fact that contacts give longer implied timescales, the folding time obtained for contacts is somewhat shorter than the result for dihedrals. This is caused by the fact that, by considering only folding events that reach state 1, fewer folding events are counted for dihedrals, see the corresponding state trajectories in Fig. 8b below.)

Showing only about thirty folding events, the finite sampling of the MD data also limits the prediction quality of the MSM. This is demonstrated in Fig. 7c which compares the histogram of folding times obtained from the MD data to distributions obtained from MSMs using various lag times. As the number of MD events is clearly too small to give a smooth distribution, it is hard to assess the true deviation of the MSM from (non-existent) statistically converged MD data.

As a standard test of the quality of the resulting MSM, we next check the validity of the Chapman-Kolmogorov equation[7]

$$T(n\tau_{\mathrm{lag}}) = T(\tau_{\mathrm{lag}})^n \tag{6}$$

with $n = 1, 2, 3, \ldots$. Assuming that we start at time $t = 0$

in a specific macrostate, we can compare the MSM prediction of the decay of this state to the corresponding results obtained from the MD data. As shown in Fig. S5b for both contacts and dihedrals, we obtain excellent agreement between MD and MSM results for most states already for relatively short lag times $\tau_{\text{lag}} \gtrsim 10\,\text{ns}$. For contacts, exceptions include the lowly (0.9 %) populated unfolded state 11, and—to a much minor extent—state 2 of the native basin, whose evolution around 100 ns is only qualitatively reproduced. For dihedrals, all states of the native basin pass the Chapman-Kolmogorov test perfectly, while the main unfolded states 11 and 12 perform only qualitatively.

Let us finally discuss the performance of the Gaussian filtering, which was introduced in Sec. 3.1 to smooth high-frequent fluctuations of the feature trajectory. To this end, we consider the implied timescales of the respective MSMs, and compare in Fig. S6a the results obtained from (i) filtering (as discussed above), (ii) dynamic coring [44,45] instead of filtering, and (iii) using no dynamic correction at all. By requesting that the trajectory spends a minimum time of 3 ns in the new state for the transition to be counted, dynamic coring overall achieves somewhat shorter timescales compared to filtering; e.g., we obtain $t_1 = 0.9$ and 1.2 µs in the case of contacts for $\tau_{\text{lag}} = 10\,\text{ns}$. Without any dynamic correction, on the other hand, the results deteriorate considerably (e.g., $t_1 = 0.7$ instead of 1.2 µs), particularly for short lag times.

Apart from improving the implied timescales of the MSM, filtering can be performed before clustering and therefore may avoid the misclassification of points in the transition regions. To study this aspect, Fig. S6b shows the contact representation of the metastable states obtained from dynamic coring, which can be compared to the results obtained for filtering (Fig. 5). Interestingly, we notice that the cored states are structurally less clearly defined than the filtered states. For contacts, for example, we find than the three main native states obtained from filtering are merged into a single cored state, and that the cored states of the unfolded basin are less distinct than their filtered counterparts. Hence, with respect to both structural characterization and slowest timescales, Gaussian filtering represents a clear improvement over dynamic coring.

4 Results on the folding of HP35

4.1 Ground truth observations

As the above described procedure to construct an MSM comes with the choice of a number of methods and associated metaparameters, it is instructive to first discuss some results obtained directly from the MD simulation. Shown in Fig. 1c, our first examples include the RMSD of the MD trajectory from the crystal structure, the percentage of native contacts Q, as well as the sum Ψ over the backbone dihedral angles ψ of the three α-helices. Constructed directly from the MD data, [43] these and related results may be considered as unbiased 'ground truth'.

We choose an upper (lower) threshold of 2 Å (6 Å) for the RMSD of folded (unfolded) conformations and employ Gaussian filtering ($\sigma = 5\,\text{ns}$), which yields 33 folding events and 32 unfolding events shown by the 300 µs trajectory. The associated free energy profile $\Delta G(\text{RMSD})$ consists of two states, showing a sharp minimum for the native state and a shallow minimum reflecting the unfolded state. Interestingly, we find that the transition path time (i.e, the time during a folding transition) of typically tens of nanoseconds is significantly shorter than the folding time (i.e, the waiting time in the unfolded state) of some microseconds. This indicates a concerted or cooperative process, where all involved coordinates change at the same time. Nonetheless, the wide barrier of $\sim 4k_{\text{B}}T$ height as well as the shallow unfolded state seem to indicate the existence of intermediate states.

Defining the percentage of formed native contacts as $Q = \sum_i \xi_i(t)/N$ (with $\xi_i(t) = 0, 1$ if contact i is broken or formed, and N being the total number of native contacts), the time evolution of $1 - Q$ is found to highly correlate with the RMSD. This holds in particular for the unfolded parts of the trajectory, while the folded parts match less. Consequently, the resulting free energy profile $\Delta G(1 - Q)$ reproduces well the unfolded part of $\Delta G(\text{RMSD})$, while it shows a somewhat broader native state. The situation is the other way round for the time evolution of Ψ representing the normalized sum of helical dihedral angles ψ, which accurately reproduces the RMSD in the native state, but exhibits considerably more fluctuations in the unfolded state. This is reflected in a sharp minimum of $\Delta G(\Psi)$ for the native state and a largely unstructured unfolded region without a minimum.

Apart from providing one-dimensional reaction coordinates, local coordinates such as contact distances and dihedral angles allow for a microscopic description of the folding process. As an example, Fig. S1a shows the time evolution of the native contacts close to a folding event. By partitioning the contacts in highly correlated MoSAIC clusters (Fig. 2), we find (as expected) that the contacts in a cluster mostly move in a concerted manner. What is more, we notice that at each folding event *all* still open contacts are formed almost simultaneously, i.e., within the transition path time of a few tens of nanoseconds. Hence, while the various clusters in general evolve differently in time, a successful folding transition involves the concerted forming of all contacts at the same time. [48] We note that this cooperative behavior may explain the relatively long folding times ($\sim 2\,\mu\text{s}$) in spite of the modest energy barriers (a few $k_{\text{B}}T$) shown by the various one-dimensional energy landscapes in Fig. 1c. Similar conclusions were also reached for the open-close functional motion of T4 lysozyme [63] and the allosteric transition in PDZ3 domain. [64]

While during a folding event all still open contacts form cooperatively within a few tens of nanoseconds, it is nonetheless interesting to study the order of the contact changes during that short time, because this might indicate a potential causal relation between the contact clusters. Figure 2c shows that typically clusters 4 and 5 (containing contacts connecting helices 2 and 3) form first, followed by cluster 6 (containing contacts at the C-terminus). On the other hand, we find that usually either cluster 7 (that connects the two terminal ends) or clusters 1, 2 and 3 (containing contacts connecting helices 1 and 2) form lastly. That is, we observe a preferred but not mandatory cluster formation order, which indicates the existence of multiple folding pathways.

Cooperative behavior is also found for the ψ-dihedral angles (Fig. S1b), which generally exhibit correlated motion within a specific helix, and move all together during a folding event. As indicated from the Leiden clustering of these angles (Fig. S2), however, the correlation of dihedral angles is overall less distinctive than for contact distances.

Recalling that the metastable states of HP35 are well characterized in terms of their contact clusters (Fig. 5), the question arises if we can turn the argument around and use

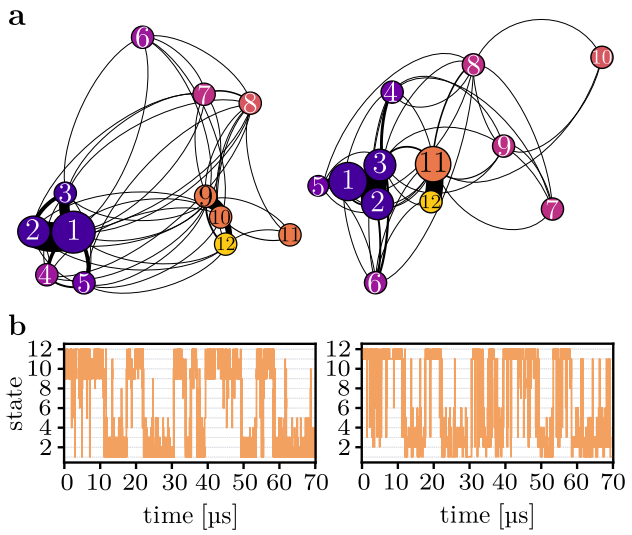

Figure 8: (a) Kinetic networks of the MSM and (b) exemplary state trajectories obtained for (left) contacts and (right) dihedrals. The node size indicates the population of the state and the color code reflects its fraction of native contacts Q (cf. Fig. 4).

the contact clusters to construct conformational states. For example, we could define a product state $(a, b, c, \ldots)$ that indicates if the various clusters a, b, c, etc. are formed or not. Alternatively, we could use dihedral angles to define a product state $(\alpha_1, \alpha_2, \alpha_3)$ indicating which helices of HP35 are formed. Various attempts along these lines to build an MSM, however, showed that representations built from contact clusters or helices are too coarse grained to yield metastable conformational states that accurately reproduce the dynamics of the system.

4.2 Kinetic network and folding pathways

By constructing the above MSMs of HP35, we found 12 metastable states with well-defined structures (Fig. 5) and their transition rates (Tab. S2). To connect these findings with the underlying folding process, it is common practice to illustrate the MSM via a network, where the node sizes correspond to the population π_i of the states and the edge weights f_{ij} to the transition probabilities T_{ij}. Since complex systems typically exhibit too many edges to visualize both transition probabilities, it is instructive to define a 'kinetic distance' between each pair of states.[84] Here we use the symmetric edge weight[46]

$$f_{ij} = \pi_i T_{ij} = \pi_j T_{ji} = f_{ji}, \tag{7}$$

which exploits the detailed balance between the two states. To optimally represent all resulting interstate distances in two dimensions, we employ the force-directed algorithm ForceAtlas2,[85] using a cut-off f_ϵ to discard small fluxes (i. e., $f_{ij} \leq f_\epsilon = 2 \times 10^{-5}$). This leads to a kinetic network representation, in which high transition rates correspond to closeness in the graph.

Figure 8a shows the resulting kinetic networks obtained for contacts and dihedrals. As anticipated from the MPP dendrograms in Fig. 4, both networks show a native basin comprising states 1 to 5 (1 to 6 for dihedrals), which is clearly separated from the unfolded basin comprising states 9 to 12 (11 to 12 for dihedrals). Moreover, several lowly populated states exist in the vicinity of the unfolded basin. To illustrate the kinetics of the networks, it is instructive to inspect the corresponding state trajectories obtained form the MD simulation (Fig. 8b). For contacts, we find fast interconversion between states 1–5 of the native basin, as well as between states 9–12 of the unfolded basin. The lowly populated states 6–8 are either temporarily visited from the unfolded basin or used as on-route intermediate states on the folding pathway. For dihedrals, we also find fast interconversion between the states (1–6) of the native basin and the states (11–12) of the unfolded basin. The lowly populated states 7–10 are mostly approached from the unfolded basin; only states 8 and 9 act in part as intermediate states for folding.

As the MSM approximates well the timescales of the system (Fig. 7a), we may illustrate various aspects of the folding process by performing Markov chain Monte Carlo simulations of the MSM. For example, by starting in the unfolded state 12 and calculating the time-dependent rise of the population of the native state 1, $P_{12\to1}(t)$, we can infer from a single exponential fit the overall folding time $t_{\text{fold}} = 1.78\,\mu\text{s}$ ($1.80\,\mu\text{s}$ for dihedrals), see Fig. 7d. (For clarity, we focus on cumulative population probabilities, i.e., we disregard all following reactions such as subsequent unfolding.) We may also study the various subprocesses underlying folding. Starting in the completely unfolded state 12, the first step is the hydrophobic collapse of the protein to the other states of the unfolded basin, where (at least) contact clusters 4 and 5 (containing contacts connecting helices 2 and 3) are formed. We note that this finding is in line with our discussion of the formation of the contact clusters in Fig. 2c. Considering the time evolution of the population of these states, $P_{12\to\text{U}}(t)$, we infer the time $t_{12\to\text{U}} = 150\,\text{ns}$ (36 ns for dihedrals) for the hydrophobic collapse. Next, we consider the time that the system remains in the unfolded basin before leaving to the native basin. Deduced from the rise of the sum of populations of all states of the native basin, $P_{12\to\text{N}}(t)$, we obtain $t_{12\to\text{N}} = 1.7\,\mu\text{s}$ ($1.6\,\mu\text{s}$ for dihedrals), indicating that the escape from the unfolded basin clearly represents the slowest step of the folding process. As a final step, we consider the system's relaxation in the native basin, i.e., the time $t_{\text{N}\to1}$ it takes after entering the native basin until state 1 is reached. Interestingly, we find that the native basin relaxation time obtained for contacts ($t_{\text{N}\to1} = 54\,\text{ns}$) is considerably shorter than the result for dihedrals ($t_{\text{N}\to1} = 370\,\text{ns}$), which reflects the higher metastability of the native states (in particular of state 2) found for dihedrals (Tab. S2).

Based on these general considerations, we now consider the main folding pathways from the completely unfolded state 12 to the native state 1, using MSMPathfinder[46] for a systematic construction of the path ensemble. Comparing the most frequented folding paths as obtained from the MD trajectory and from the MSM, Tab. S3 reveals good overall agreement between the results of MD and MSM. For contacts, in most cases (26 out of 34 in MD) the system first goes to state 10. Moreover, we find six first transitions to state 9, as well as two direct transitions to state 5 in the native basin. As discussed above, the system subsequently spends most of the folding time t_{fold} in the unfolded basin, before it changes to the native basin via a concerted forming of all still open contacts. That is, the broad distribution of folding times shown in Figs. 7b,c originates mostly from different escape times $t_{\text{U}\to\text{N}}$. While we obtain similar results for dihedrals, we note that the description of the unfolded basin is less well resolved. That is, from completely unfolded state 12 the first step goes with only a single exception to state 11,

from where the native basin is approached.

Compared to the experimental result (0.73 µs at 360 K for the considered Nle/Nle-mutant [35]), the MD simulation of Piana et al. [43] overestimates the overall folding time by a factor 2.5. Moreover, various experiments [34–36] reported a fast (~ 0.1 µs) transient, which was interpreted as relaxation in the unfolded basin or in the folded basin. This compares roughly to the associated timescales $t_{12\to U}$ and $t_{N\to 1}$ discussed above. Relating the factor 2.5 to a free energy difference Δ via $2.5 = e^{\Delta/k_B T}$, we infer a quite low overall error $\Delta \sim 2.8$ kJ/mol of the employed force field, which is in line with previous studies. [86,87] Nonetheless, this accuracy of biomolecular force fields appears surprisingly good, in particular when we consider energy barrier heights associated with microsecond timescales. This finding might be a consequence of folding being eventually mediated by the forming of interresidue contacts (which should be well described by common force fields) and the relatively long folding times are related to the finding that a successful folding transition involves the concerted forming of all contacts that are still open.

5 Discussion

5.1 Feature selection: Contacts vs. dihedrals

Adopting the ultrafast folding of HP35 as well-established model problem, we have studied the virtues and shortcomings of using backbone dihedral angles or contact distances as features to construct an MSM. While dihedral angles are readily obtained from the MD trajectory, they require an appropriate treatment of their periodicity [65–67] and necessitate the exclusion of uncorrelated dihedral motion. Following recent work, [46,66] here we used maximal-gap shifted (ϕ, ψ) dihedral angles and excluded the terminal residues 1–2 and 34–35. With ψ-angles reflecting the helicity of the protein and ϕ-angles accounting for potential left-to-right handed transitions (mainly in flexible loops), backbone dihedral angles report directly on the local secondary structure. This proves advantageous for the modeling of the conformational states in the native basin of HP35, which can be mainly described by the single angle ϕ_3 (Fig. S4c). However, dihedral angles account only indirectly for the formation of tertiary structure during folding, which hampers the modeling of the folding transition and the conformational distribution in the unfolded basin.

Considering contacts, on the other hand, we have found that their selection and appropriate calculation of the corresponding contact distances requires some attention. By introducing a new definition of contact distances [Eq. (2)], we focused on the native contacts of HP35, because they are expected to largely determine the folding pathways. [56–58] Performing a correlation analysis [32] on the resulting 42 native contacts, we identified seven clusters (Fig. 2), whose contacts are highly correlated and change in a concerted manner. These contact clusters were shown to directly account for the cooperative folding of HP35 (Fig. S1a), and also provide a concise characterization of the metastable states of the system (Fig. 5). In particular, tertiary contacts were shown to be key to the folding process, because they represent the most direct descriptor of the origin of folding. As a consequence, the first implied timescales of the MSMs obtained for contacts (e.g., $t_1 = 1.2$ µs for $\tau_{lag} = 10$ ns) are significantly slower than the corresponding results obtained for dihedrals (0.7 µs), indicating that contacts overall give a better Markovian model than dihedrals. Hence, reflecting different aspects of the structural dynamics, contacts and dihedrals result in different collective variables and metastable states, eventually leading to MSMs with different timescales and pathways.

5.2 MSM workflow: What matters?

While we have stressed the importance of the selection of features, the discussion of the results obtained from the MSM inevitably rests on the specific techniques employed for its construction, including various methods of dynamic correction, dimensionality reduction, and clustering. To briefly summarize what parts of the procedure made a difference, we focus on the case of contacts in the following.

Although a number of more sophisticated methods is available, [69–71] we suppose that standard linear PCA is sufficient for the present case study (provided that appropriate features are available). Including the first five components, PCA was shown to explain the majority (80 %) of the correlation and to account well for the slowest timescales (Fig. S3). As a benefit, linear methods produce smoothly varying free energy landscapes, which facilitate the subsequent clustering. For the latter we adopted robust density-based clustering [68] as an accurate and efficient deterministic method to construct microstates. Presumably, the popular k-means method should give clusterings of similar overall quality, provided that the required metaparameters (such as the number of states k) are optimized and that sufficiently many iterations are run. [88]

Apart from these commonly used methods, we want to point out two simple and powerful techniques, which are less widely known but clearly improved the outcome of the MSM. First of all, we used Gaussian low-pass filtering to smoothen high-frequent fluctuations of the feature trajectory, which significantly reduced spurious transitions between adjacent metastable states. While the idea is similar to the definition of dynamic cores of the metastable states [44,45] (where we request that the trajectory spends a minimum time in the new state for the transition to be counted), the filtering is performed before the clustering and therefore helps to avoid the misclassification of points in the transition regions.

Secondly, we want to highlight the explanatory power of the dendrograms constructed from MPP clustering (Fig. 4). Revealing how the metastable states emerge from the microstates, the MPP dendrogram outlines the hierarchical structure of the free energy landscape. [72] For example, we learn that the unfolded part of the energy landscape of HP35 is structured and reveals several metastable states with lifetimes of about 40 ns (Tab. S2). Furthermore, we notice that the dendrogram for dihedrals exhibits two rather metastable subsections of the native basin, which explain the relatively long relaxation time found for this basin (Fig. 7). By coloring the microstates according to their mean number of native contacts Q, we may assess if only structurally similar states are merged together, thus illustrating the quality of the state partitioning. Last but not least, the MPP dendrogram is closely related to the kinetic network (Fig. 8) that nicely illustrates the overall dynamics exhibited by the MSM.

6 Concluding remarks

By designing an MSM, we aim to construct structurally well-defined metastable states that provide a mechanistic understanding of the considered biomolecular process. Adopting the folding of HP35 as a textbook example, we have highlighted several important aspects for the practical construction of an MSM.

- First, the overall quality of a dynamical model such as an MSM relies on the selection of input coordinates or features, which faithfully account for the process under consideration. Inclusion of deceiving coordinates or the omission of important features will quite certainly corrupt subsequent analyses. We have employed a correlation analysis strategy to identify appropriate features,[32] and discussed in detail two main types, that is, interresidue contacts and backbone dihedral angles.
- A successful state partitioning should provide conformational states that are clearly discriminated by some descriptors derived from the features, such as the mean and the variance of the contact cluster distributions (Fig. 5). The quality of the state partitioning can be furthermore assessed by the MPP dendrogram (Fig. 4), which reveals potential conformational heterogeneity of the microstates being merged to a macrostate.
- Dynamical corrections such as low-pass filtering of the feature trajectory and the optimal projection of microstate dynamics onto macrostate dynamics[73,80–83] may significantly improve the Markovianity of the MSM.

Proceeding this way, we have obtained MSMs describing the folding of HP35, which correctly reproduce the slow timescales of the process. This result is not achieved by design, but indicates a consistent dynamical model. Alternatively, we may construct an MSM by requesting long timescales from the outset.[12,13] While this approach may simplify the construction of the MSM, it still needs to be checked if the resulting metastable states are structurally well characterized and do provide the desired mechanistic understanding of the process.

Acknowledgement The authors thank Georg Diez, Matthias Post and Steffen Wolf for helpful comments and discussions, as well as D. E. Shaw Research for sharing their trajectories of HP35. This work has been supported by the Deutsche Forschungsgemeinschaft (DFG) within the framework of the Research Unit FOR 5099 "Reducing complexity of nonequilibrium" (project No. 431945604), the High Performance and Cloud Computing Group at the Zentrum für Datenverarbeitung of the University of Tübingen, the state of Baden-Württemberg through bwHPC and the DFG through grant no INST 37/935-1 FUGG (RV bw16I016), and the Black Forest Grid Initiative.

Data Availability Statement

The simulation data and all intermediate results, including our Python package msmhelper and detailed descriptions to reproduce all steps of the analyses, can be downloaded from https://github.com/moldyn/HP35. In particular, we provide trajectories (300 µs long, 1.5×10^6 data points) of (1) the three discussed definitions of contact distances, (2) the maximal-gap shifted dihedral angles, (3) the resulting principal components, and (4) the resulting micro- and macrostates.

Supporting Information Available

Tables of the native contacts of HP35, as well as of the transition matrices and folding pathways obtained for contacts and dihedral angles. Figures of the cooperative transition of contacts and dihedral angles, the correlation analysis for dihedral angels, details on PCA and clustering, and the Chapman-Kolmogorov tests.

References

(1) Berendsen, H. J. C. *Simulating the Physical World*; Cambridge University Press: Cambridge, 2007.
(2) Lange, O. F.; Grubmüller, H. Collective Langevin dynamics of conformational motions in proteins. *J. Chem. Phys.* **2006**, *124*, 214903.
(3) Hegger, R.; Stock, G. Multidimensional Langevin modeling of biomolecular dynamics. *J. Chem. Phys.* **2009**, *130*, 034106.
(4) Ayaz, C.; Tepper, L.; Brünig, F. N. et al. Non-Markovian modeling of protein folding. *Proc. Natl. Acad. Sci. USA* **2021**, *118*, e2023856118.
(5) Buchete, N.-V.; Hummer, G. Coarse master equations for peptide folding dynamics. *J. Phys. Chem. B* **2008**, *112*, 6057–6069.
(6) Bowman, G. R.; Beauchamp, K. A.; Boxer, G. et al. Progress and challenges in the automated construction of Markov state models for full protein systems. *J. Chem. Phys.* **2009**, *131*, 124101.
(7) Prinz, J.-H.; Wu, H.; Sarich, M. et al. Markov models of molecular kinetics: generation and validation. *J. Chem. Phys.* **2011**, *134*, 174105.
(8) Bowman, G. R.; Pande, V. S.; Noé, F. *An Introduction to Markov State Models*; Springer: Heidelberg, 2013.
(9) Wang, W.; Cao, S.; Zhu, L. et al. Constructing Markov State Models to elucidate the functional conformational changes of complex biomolecules. *WIREs Comp. Mol. Sci.* **2017**, *8*, e1343.
(10) Scherer, M. K.; Trendelkamp-Schroer, B.; Paul, F. et al. PyEMMA 2: A Software Package for Estimation, Validation, and Analysis of Markov Models. *J. Chem. Theory Comput.* **2015**, *11*, 5525.
(11) Beauchamp, K. A.; Bowman, G. R.; Lane, T. J. et al. MSMBuilder2: Modeling Conformational Dynamics on the Picosecond to Millisecond Scale. *J. Chem. Theory Comput.* **2011**, *7*, 3412–3419.
(12) Nüske, F.; Keller, B. G.; Perez-Hernández, G. et al. Variational Approach to Molecular Kinetics. *J. Chem. Theory Comput.* **2014**, *10*, 1739–1752.
(13) Wu, H.; Noé, F. Learning Markov Processes from Time Series Data. *J. Nonlinear. Sci.* **2020**, *30*, 23–66.
(14) Sittel, F.; Stock, G. Perspective: Identification of Collective Coordinates and Metastable States of Protein Dynamics. *J. Chem. Phys.* **2018**, *149*, 150901.
(15) Scherer, M. K.; Husic, B. E.; Hoffmann, M. et al. Variational selection of features for molecular kinetics. *J. Chem. Phys.* **2019**, *150*, 194108.
(16) Konovalov, K. A.; Unarta, I. C.; Cao, S. et al. Markov State Models to Study the Functional Dynamics of Proteins in the Wake of Machine Learning. *JACS Au* **2021**, *1*, 1330–1341.
(17) As the commonly employed rotational fit of the Cartesian trajectory to a reference structure cannot entirely remove the overall rotation of a flexible system, the residual overall rotation may completely destroy the outcome of a subsequent dimensionality reduction.[19] Interestingly, this breakdown may be not obvious, when we select input coordinates by maximizing the slowest timescales[15].

(18) Mu, Y.; Nguyen, P. H.; Stock, G. Energy Landscape of a Small Peptide Revealed by Dihedral Angle Principal Component Analysis. *Proteins* **2005**, *58*, 45 – 52.

(19) Sittel, F.; Jain, A.; Stock, G. Principal component analysis of molecular dynamics: On the use of Cartesian vs. internal coordinates. *J. Chem. Phys.* **2014**, *141*, 014111.

(20) Altis, A.; Otten, M.; Nguyen, P. H. et al. Construction of the free energy landscape of biomolecules via dihedral angle principal component analysis. *J. Chem. Phys.* **2008**, *128*, 245102.

(21) Maisuradze, G. G.; Liwo, A.; Scheraga, H. A. Principal Component Analysis for Protein Folding Dynamics. *J. Mol. Biol.* **2009**, *385*, 312 – 329.

(22) Riccardi, L.; Nguyen, P. H.; Stock, G. Free energy landscape of an RNA hairpin constructed via dihedral angle principal component analysis. *J. Phys. Chem. B* **2009**, *113*, 16660 – 16668.

(23) Fenwick, R. B.; Orellana, L.; Esteban-Martín, S. et al. Correlated motions are a fundamental property of β-sheets. *Nat. Commun.* **2014**, *5*, 4070.

(24) Lätzer, J.; Shen, T.; Wolynes, P. G. Conformational Switching upon Phosphorylation: A Predictive Framework Based on Energy Landscape Principles. *Biochem.* **2008**, *47*, 2110–2122.

(25) Hori, N.; Chikenji, G.; Berry, R. S. et al. Folding energy landscape and network dynamics of small globular proteins. *Proc. Natl. Acad. Sci. USA* **2009**, *106*, 73–78.

(26) Kalgin, I. V.; Caflisch, A.; Chekmarev, S. F. et al. New Insights into the Folding of a beta-Sheet Miniprotein in a Reduced Space of Collective Hydrogen Bond Variables: Application to a Hydrodynamic Analysis of the Folding Flow. *J. Phys. Chem. B* **2013**, *117*, 6092–6105.

(27) Ernst, M.; Sittel, F.; Stock, G. Contact- and distance-based principal component analysis of protein dynamics. *J. Chem. Phys.* **2015**, *143*, 244114.

(28) Ernst, M.; Wolf, S.; Stock, G. Identification and validation of reaction coordinates describing protein functional motion: Hierarchical dynamics of T4 Lysozyme. *J. Chem. Theory Comput.* **2017**, *13*, 5076 – 5088.

(29) Oide, M.; Sugita, Y. Protein folding intermediates on the dimensionality reduced landscape with UMAP and native contact likelihood. *J. Chem. Phys.* **2022**, *157*, 075101.

(30) Amadei, A.; Linssen, A. B. M.; Berendsen, H. J. C. Essential dynamics of proteins. *Proteins* **1993**, *17*, 412–425.

(31) Perez-Hernandez, G.; Paul, F.; Giorgino, T. et al. Identification of slow molecular order parameters for Markov model construction. *J. Chem. Phys.* **2013**, *139*, 015102.

(32) Diez, G.; Nagel, D.; Stock, G. Correlation-based feature selection to identify functional dynamics in proteins. *J. Chem. Theory Comput.* **2022**, *18*, 5079 – 5088.

(33) Chiu, T. K.; Kubelka, J.; Herbst-Irmer, R. et al. High-resolution x-ray crystal structures of the villin headpiece subdomain, an ultrafast folding protein. *Proc. Natl. Acad. Sci. USA* **2005**, *102*, 7517–7522.

(34) Brewer, S.; Song, B.; Raleigh, D. et al. Residue Specific Resolution of Protein Folding Dynamics Using Isotope-Edited Infrared Temperature Jump Spectroscopy. *Biochem.* **2007**, *46*, 3279–3285.

(35) Kubelka, J.; Chiu, T. K.; Davies, D. R. et al. Sub-microsecond protein folding. *J. Mol. Biol.* **2006**, *359*, 546–553.

(36) Kubelka, J.; Henry, E. R.; Cellmer, T. et al. Chemical, physical, and theoretical kinetics of an ultrafast folding protein. *Proc. Natl. Acad. Sci. USA* **2008**, *105*, 18655–18662.

(37) Reiner, A.; Henklein, P.; Kiefhaber, T. An unlocking/relocking barrier in conformational fluctuations of villin headpiece subdomain. *Proc. Natl. Acad. Sci. USA* **2010**, *107*, 4955 – 4960.

(38) Duan, Y.; Kollman, P. A. Pathways to a protein folding intermediate observed in a 1-microsecond simulation in aqueous solution. *Science* **1998**, *282*, 740–744.

(39) Snow, C. D.; Nguyen, H.; Pande, V. S. et al. Absolute comparison of simulated and experimenta protein folding dynamics. *Nature (London)* **2002**, *420*, 102.

(40) Ensign, D. L.; Kasson, P. M.; Pande, V. S. Heterogeneity even at the speed limit of folding: large-scale molecular dynamics study of a fast-folding variant of the villin headpiece. *J. Mol. Biol.* **2007**, *374*, 806–816.

(41) Rajan, A.; Freddolino, P. L.; Schulten, K. Going beyond clustering in MD trajectory analysis: an application to villin headpiece folding. *PLoS One* **2010**, *5*, e9890.

(42) Beauchamp, K. A.; Ensign, D. L.; Das, R. et al. Quantitative comparison of villin headpiece subdomain simulations and triplet–triplet energy transfer experiments. *Proc. Natl. Acad. Sci. USA* **2011**, *108*, 12734 – 12739.

(43) Piana, S.; Lindorff-Larsen, K.; Shaw, D. E. Protein folding kinetics and thermodynamics from atomistic simulation. *Proc. Natl. Acad. Sci. USA* **2012**, *109*, 17845–17850.

(44) Jain, A.; Stock, G. Hierarchical folding free energy landscape of HP35 revealed by most probable path clustering. *J. Phys. Chem. B* **2014**, *118*, 7750 – 7760.

(45) Nagel, D.; Weber, A.; Lickert, B. et al. Dynamical coring of Markov state models. *J. Chem. Phys.* **2019**, *150*, 094111.

(46) Nagel, D.; Weber, A.; Stock, G. MSMPathfinder: Identification of pathways in Markov state models. *J. Chem. Theory Comput.* **2020**, *16*, 7874 – 7882.

(47) Sormani, G.; Rodriguez, A.; Laio, A. Explicit Characterization of the Free-Energy Landscape of a Protein in the Space of All Its C_α Carbons. *J. Chem. Theory Comput.* **2020**, *16*, 80–87.

(48) Chong, S.-H.; Ham, S. Time-dependent communication between multiple amino acids during protein folding. *Chem. Sci.* **2021**, *12*, 5944–5951.

(49) Hornak, V.; Abel, R.; Okur, A. et al. Comparison of multiple Amber force fields and development of improved protein backbone parameters. *Proteins* **2006**, *65*, 712–725.

(50) Best, R. B.; Hummer, G. Optimized Molecular Dynamics Force Fields Applied to the Helix-Coil Transition of Polypeptides. *J. Phys. Chem. B* **2009**, *113*, 9004–9015.

(51) Lindorff-Larsen, K.; Piana, S.; Palmo, K. et al. Improved side-chain torsion potentials for the Amber ff99SB protein force field. *Proteins* **2010**, *78*, 1950 – 1958.

(52) Jorgensen, W. L.; Chandrasekhar, J.; Madura, J. D. et al. Comparison of simple potential functions for simulating liquid water. *J. Chem. Phys.* **1983**, *79*, 926.

(53) As shown in Tab. S1, we get 42 contacts from Eq. (2) and 50 from Eq. (1).

(54) Heringa, J.; Argos, P. Side-chain clusters in protein structures and their role in protein folding. *J. Mol. Biol.* **1991**, *220*, 151 – 171.

(55) Yao, X.-Q.; Momin, M.; Hamelberg, D. Establishing a Framework of Using Residue–Residue Interactions in Protein Difference Network Analysis. *J. Chem. Inf. Model.* **2019**, *59*, 3222–3228.

(56) Sali, A.; Shakhnovich, E.; Karplus, M. How does a protein fold? *Nature (London)* **1994**, *369*, 248 – 251.

(57) Wolynes, P. G.; Onuchic, J. N.; Thirumalai, D. Navigating the Folding Routes. *Science* **1995**, *267*, 1619–1620.

(58) Best, R. B.; Hummer, G.; Eaton, W. A. Native contacts determine protein folding mechanisms in atomistic simulations. *Proc. Natl. Acad. Sci. USA* **2013**, *110*, 17874–17879.

(59) Best, R. B.; Hummer, G. Coordinate-dependent diffusion in protein folding. *Proc. Natl. Acad. Sci. USA* **2010**, *107*, 1088 – 1093.

(60) Lange, O. F.; Grubmüller, H. Generalized Correlation for Biomolecular Dynamics. *Proteins* **2006**, *62*, 1053–1061.

(61) Traag, V.; Waltman, L.; van Eck, N. From Louvain to Leiden: guaranteeing well-connected communities. *Sci. Rep.* **2019**, *9*, 5233.

(62) Buchenberg, S.; Schaudinnus, N.; Stock, G. Hierarchical biomolecular dynamics: Picosecond hydrogen bonding regulates microsecond conformational transitions. *J. Chem. Theory Comput.* **2015**, *11*, 1330–1336.

(63) Post, M.; Lickert, B.; Diez, G. et al. Cooperative protein allosteric transition mediated by a fluctuating transmission network. *J. Mol. Bio.* **2022**, *434*, 167679.

(64) Ali, A. A. A. I.; Gulzar, A.; Wolf, S. et al. Nonequilibrium modeling of the elementary step in PDZ3 allosteric communication. *J. Phys. Chem. Lett.* **2022**, *13*, 9862 – 9868.

(65) Altis, A.; Nguyen, P. H.; Hegger, R. et al. Dihedral angle principal component analysis of molecular dynamics simulations. *J. Chem. Phys.* **2007**, *126*, 244111.

(66) Sittel, F.; Filk, T.; Stock, G. Principal component analysis on a torus: Theory and application to protein dynamics. *J. Chem. Phys.* **2017**, *147*, 244101.

(67) Zouboulоglou, P.; García-Portugués, E.; Marron, J. S. Scaled Torus Principal Component Analysis. *J. Comput. Graph. Stat.* **2022**, *0*, 1–12.
(68) Sittel, F.; Stock, G. Robust Density-Based Clustering to Identify Metastable Conformational States of Proteins. *J. Chem. Theory Comput.* **2016**, *12*, 2426–2435.
(69) Rohrdanz, M. A.; Zheng, W.; Clementi, C. Discovering Mountain Passes via Torchlight: Methods for the Definition of Reaction Coordinates and Pathways in Complex Macromolecular Reactions. *Annu. Rev. Phys. Chem.* **2013**, *64*, 295–316.
(70) Wang, Y.; Lamim Ribeiro, J. M.; Tiwary, P. Machine learning approaches for analyzing and enhancing molecular dynamics simulations. *Curr. Opin. Struct. Biol.* **2020**, *61*, 139–145.
(71) Glielmo, A.; Husic, B. E.; Rodriguez, A. et al. Unsupervised Learning Methods for Molecular Simulation Data. *Chem. Rev.* **2021**, *121*, 9722–9758.
(72) Jain, A.; Stock, G. Identifying metastable states of folding proteins. *J. Chem. Theory Comput.* **2012**, *8*, 3810 – 3819.
(73) Hummer, G.; Szabo, A. Optimal Dimensionality Reduction of Multistate Kinetic and Markov-State Models. *J. Phys. Chem. B* **2015**, *119*, 9029–9037.
(74) Schütte, C.; Noé, F.; Lu, J. et al. Markov state models based on milestoning. *J. Chem. Phys.* **2011**, *134*, 204105.
(75) Lemke, O.; Keller, B. G. Density-based cluster algorithms for the identification of core sets. *J. Chem. Phys.* **2016**, *145*, 164104.
(76) In general, we find that different energy basins have different metastabilities, making it inappropriate to split the dendrogram at a constant value of $Q_{\min}$. As a remedy, the MPP algorithm was extended to automatically detect branches, by considering both a minimum population $P_{\min}$ and a minimum metastability $Q_{\min}$. Branches are evaluated in a top-down fashion, with sub-branches being considered in case they meet the minimum criteria. Once all branches have been processed, any remaining microstates are assigned to their dynamically nearest macrostate.
(77) In fact, these conditions produced 13 (instead of 12) contacts-based states. Since the additional state 13 (on the very left side of the dendrogram) is completely unfolded just like state 12, however, we simply may merge them into a single state when we discuss folding. This facilitates the comparison with the 12 dihedral-based states .
(78) Brandt, S.; Sittel, F.; Ernst, M. et al. Machine Learning of Biomolecular Reaction Coordinates. *J. Phys. Chem. Lett.* **2018**, *9*, 2144 – 2150.
(79) Chen, T.; Guestrin, C. XGBoost: A Scalable Tree Boosting System. *CoRR* **2016**, abs/1603.02754.
(80) Kells, A.; Mihalka, Z. E.; Annibale, A. et al. Mean first passage times in variational coarse graining using Markov state models. *J. Chem. Phys.* **2019**, *150*, 134107.
(81) Reuter, B.; Fackeldey, K.; Weber, M. Generalized Markov modeling of nonreversible molecular kinetics. *J. Chem. Phys.* **2019**, *150*, 174103.
(82) Cao, S.; Montoya-Castillo, A.; Wang, W. et al. On the advantages of exploiting memory in Markov state models for biomolecular dynamics. *J. Chem. Phys.* **2020**, *153*, 014105.
(83) Sharpe, D. J.; Wales, D. J. Nearly reducible finite Markov chains: Theory and algorithms. *J. Chem. Phys.* **2021**, *155*, 140901.
(84) Noé, F.; Banisch, R.; Clementi, C. Commute Maps: Separating Slowly Mixing Molecular Configurations for Kinetic Modeling. *J. Chem. Theory Comput.* **2016**, *12*, 5620–5630.
(85) Jacomy, M.; Venturini, T.; Heymann, S. et al. ForceAtlas2, a Continuous Graph Layout Algorithm for Handy Network Visualization Designed for the Gephi Software. *PLOS ONE* **2014**, *9*, 1–12.
(86) Mittal, J.; Best, R. B. Tackling Force-Field Bias in Protein Folding Simulations: Folding of Villin HP35 and Pin WW Domains in Explicit Water. *Biophys. J.* **2010**, *99*, L26–L28.
(87) Piana, S.; Lindorff-Larsen, K.; Shaw, D. E. How Robust Are Protein Folding Simulations with Respect to Force Field Parameterization? *Biophys. J.* **2011**, *100*, L47 – L49.
(88) Husic, B. E.; McGibbon, R. T.; Sultan, M. M. et al. Optimized parameter selection reveals trends in Markov state models for protein folding. *J. Chem. Phys.* **2016**, *145*, 194103.

arXiv:2303.03814v1 [q-bio.BM] 7 Mar 2023

Supporting Information: Selecting Features for Markov Modeling: A Case Study on HP35

Daniel Nagel, Sofia Sartore, and Gerhard Stock*

Biomolecular Dynamics, Institute of Physics, Albert-Ludwigs-Universität, 79104 Freiburg, Germany.

E-mail: stock@physik.uni-freiburg.de

Table S1: Native contacts of HP35, as obtained from the crystal structure[S1] (left) and from the MD simulation by Piana et al.,[S2] where the minimum contact distance is defined via Eq. (1) of the main text (middle, MD contacts I), and via Eq. (2) but omitting atom pairs not satisfying the population cutoff of 30 % (right, MD contacts II). For each contact definition and each contact, we list the percentage of the simulation time when the contact is formed, as well as the decay time τ of the contact autocorrelation function $C_{ij}(t) = \langle \delta d_{ij}(t) \delta d_{ij}(0) \rangle / \langle \delta d_{ij}^2 \rangle$, i.e. $C_{ij}(\tau) = 1/e$. The contact type is assigned as helical if it is a helix-stabilizing $(n, n+4)$ contact, as hydrogen bond if both residues have oppositely charged side chains, and as hydrophobic else.

residues	contact type	MoSAIC cluster	crystal contacts formed [%]	crystal contacts τ [µs]	MD contacts I formed [%]	MD contacts I τ [µs]	MD contacts II formed [%]	MD contacts II τ [µs]
LEU1–ASP5	helical	–	11.5	0.019	39.8	0.009	–	–
LEU1–PHE6	hydrophobic	–	2.1	0.027	–	–	–	–
LEU1–VAL9	hydrophobic	–	3.2	0.034	–	–	–	–
LEU1–PHE10	hydrophobic	–	1.9	0.030	–	–	–	–
LEU1–ARG14	hydrophobic	–	7.3	0.527	–	–	–	–
LEU1–LEU34	hydrophobic	–	3.7	0.030	–	–	–	–
SER2–PHE6	hydrogen bond	–	29.7	0.039	35.7	0.048	–	–
ASP3–LYS7	helical	8	71.0	0.092	75.8	0.050	74.7	0.072
ASP3–THR13	hydrophobic	1	–	–	56.9	1.380	46.5	1.574
ASP3–ARG14	hydrogen bond	1	29.2	1.104	69.6	1.210	61.6	1.466
GLU4–ALA8	helical	8	63.0	0.055	65.6	0.048	65.0	0.055
ASP5–VAL9	helical	8	54.7	0.080	69.6	0.108	67.1	0.150
ASP5–ARG14	hydrogen bond	1	–	–	49.9	0.241	47.2	0.471
PHE6–PHE10	helical	8	74.8	0.679	80.4	0.413	75.7	0.589
PHE6–GLY11	hydrophobic	2	56.9	0.639	60.4	0.348	56.9	0.639
PHE6–MET12	hydrophobic	2	25.9	1.481	74.1	0.998	63.6	1.558
PHE6–THR13	hydrophobic	–	16.4	1.366	61.5	0.806	–	–
PHE6–ARG14	hydrophobic	1	24.2	1.481	73.7	0.948	69.4	1.339
PHE6–PHE17	hydrophobic	2	42.9	1.408	70.0	1.071	57.5	1.352
LYS7–GLY11	hydrogen bond	2	71.6	0.929	74.1	0.798	72.7	0.857
LYS7–MET12	hydrophobic	2	66.0	1.725	73.3	0.958	70.1	1.222
LYS7–THR13	hydrophobic	2	16.4	1.481	55.0	0.672	33.5	1.481
VAL9–LYS32	hydrophobic	7	50.7	1.380	60.0	1.222	54.7	1.380
VAL9–LEU34	hydrophobic	–	22.1	0.840	36.2	0.452	–	–
PHE10–PHE17	hydrophobic	–	20.6	1.352	62.0	0.874	–	–
PHE10–LEU28	hydrophobic	–	27.6	1.380	67.5	1.138	–	–
PHE10–NLE29	hydrophobic	7	16.4	1.352	59.6	0.892	36.0	1.380
PHE10–LYS32	hydrophobic	–	20.2	1.352	55.2	1.150	–	–
PHE10–LEU34	hydrophobic	7	33.8	1.060	47.3	0.554	33.8	1.060
MET12–ALA16	hydrophobic	3	49.4	1.298	72.8	0.141	61.9	1.071
MET12–PHE17	hydrophobic	3	52.9	1.394	74.3	0.560	61.5	1.234
MET12–LEU20	hydrophobic	3	42.3	1.272	56.4	0.766	52.4	1.272
MET12–LEU28	hydrophobic	–	18.8	1.173	32.5	0.743	–	–
THR13–PHE17	hydrogen bond	3	78.0	1.312	80.9	1.060	78.4	1.312
ARG14–ALA18	helical	8	77.5	1.298	79.4	0.939	78.1	1.222
SER15–ASN19	helical	8	69.1	0.613	78.0	0.256	73.4	0.589
ALA16–LEU20	hydrogen bond	8	72.3	0.120	80.4	0.066	79.5	0.092
PHE17–GLN25	hydrophobic	4	83.2	0.665	87.7	0.537	86.7	0.626
PHE17–LEU28	hydrophobic	–	24.9	0.645	71.0	0.665	–	–
PHE17–NLE29	hydrophobic	8	32.3	0.883	58.3	0.543	48.2	0.848
ALA18–GLN25	hydrophobic	4	62.6	0.506	80.3	0.501	79.1	0.537
LEU20–NLE24	hydrogen bond	8	27.5	0.036	81.3	0.012	56.5	0.053
LEU20–GLN25	hydrophobic	4	86.8	0.249	93.2	0.105	89.9	0.244
LEU20–LEU28	hydrophobic	5	54.2	0.532	70.8	0.405	54.2	0.532
PRO21–GLN25	hydrogen bond	8	97.2	0.107	98.0	0.081	97.8	0.088
LEU22–GLN26	helical	8	95.4	0.099	96.7	0.074	96.5	0.081
TRP23–HIS27	helical	8	90.8	0.121	93.1	0.088	91.5	0.117
NLE24–LEU28	helical	5	89.3	0.287	90.9	0.225	90.2	0.262
GLN25–NLE29	helical	5	87.5	0.645	88.8	0.589	88.1	0.639
GLN26–LYS30	helical	8	81.6	0.751	84.1	0.658	83.0	0.729
GLN26–PHE35	hydrophobic	–	–	–	56.3	0.086	–	–
HIS27–GLU31	helical	8	77.9	0.413	83.3	0.134	81.1	0.222
LEU28–LYS32	helical	8	77.0	0.147	80.4	0.108	78.7	0.142
NLE29–GLY33	hydrogen bond	6	74.2	0.112	77.2	0.082	74.6	0.108
NLE29–LEU34	hydrogen bond	6	66.5	0.161	75.1	0.088	67.9	0.130
NLE29–PHE35	hydrophobic	6	4.9	0.081	67.2	0.073	60.3	0.119
LYS30–PHE35	hydrophobic	6	–	–	66.3	0.054	52.9	0.113

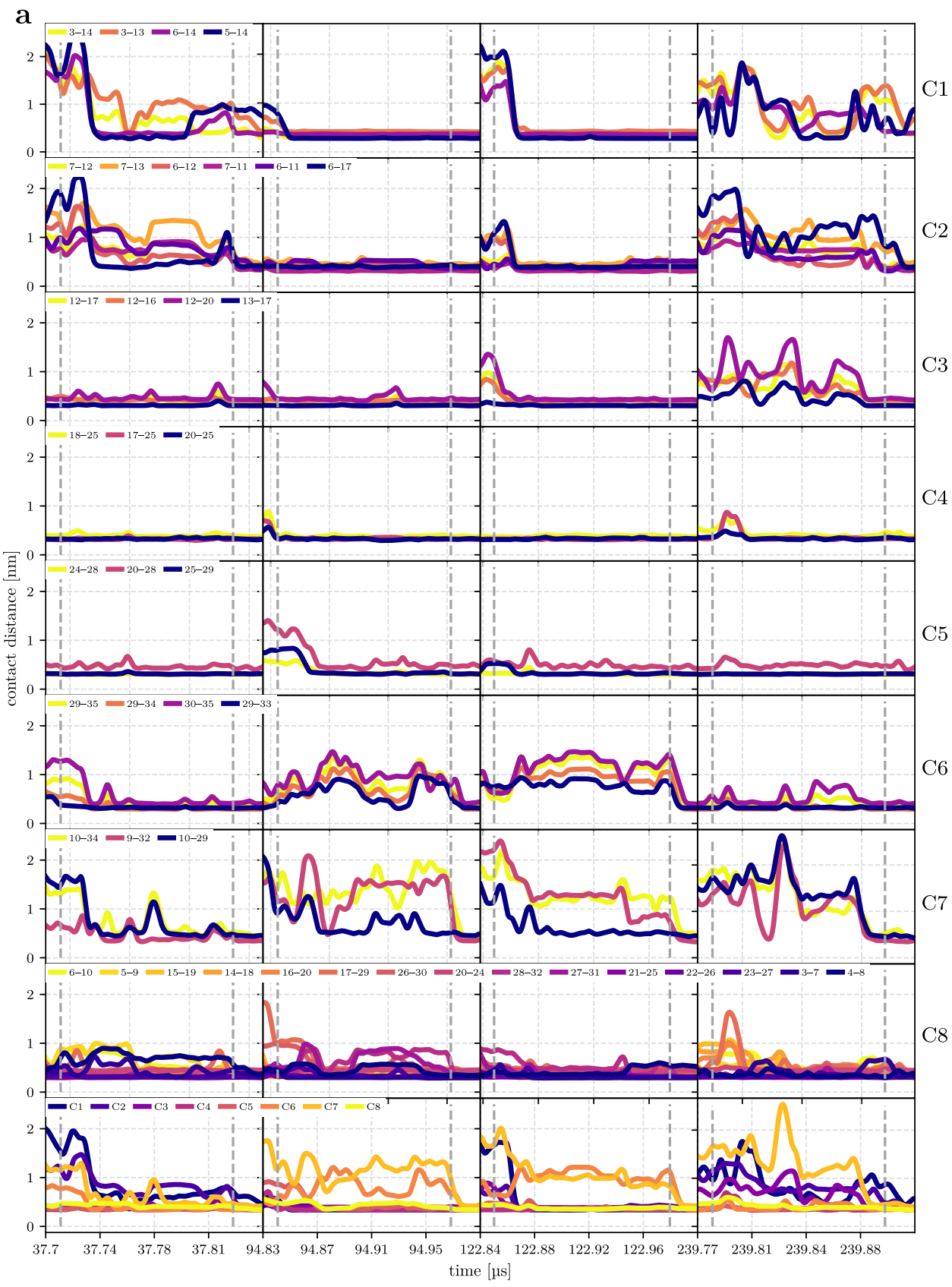
a
3–14 3–13 6–14 5–14
7–12 7–13 6–12 7–11 6–11 6–17
12–17 12–16 12–20 13–17
18–25 17–25 20–25
24–28 20–28 25–29
29–35 29–34 30–35 29–33
10–34 9–32 10–29
6–10 5–9 15–19 14–18 16–20 17–29 26–30 20–24 28–32 27–31 21–25 22–26 23–27 3–7 4–8
C1 C2 C3 C4 C5 C6 C7 C8
C1
C2
C3
C4
C5
C6
C7
C8
contact distance [nm]
0
1
2
37.7
37.74
37.78
37.81
94.83
94.87
94.91
94.95
122.84
122.88
122.92
122.96
239.77
239.81
239.84
239.88
time [µs]

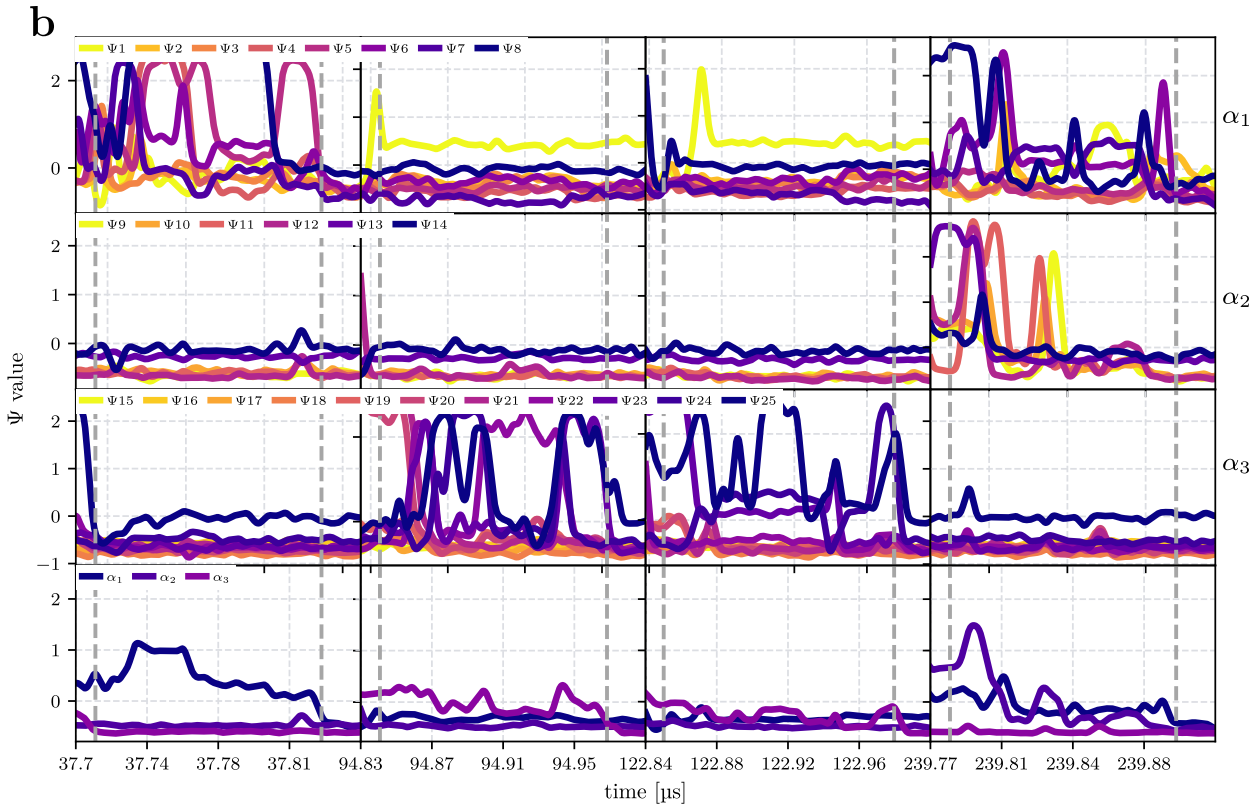

Figure S1: Cooperative behavior of input features during 4 randomly selected folding events, identified with RMSD thresholds, for (a) contacts and (b) dihedral angles. The contacts are grouped by MoSAIC clusters and the figure shows that distances belonging to the same cluster move together and 'jump' at the same time below the contact threshold of 4.5 Å. Moreover, one can see that some clusters (cluster 4 and cluster 5, featuring contacts connecting helix 2 and helix 3 and contacts belonging to the third helix) are most times already formed very early on. This is in good agreement with Fig. 2c showing the order of clusters formation. Dihedrals are grouped by helices and they also show cooperativity within the secondary structure they belong to, although they are not as correlated as in the contacts case.

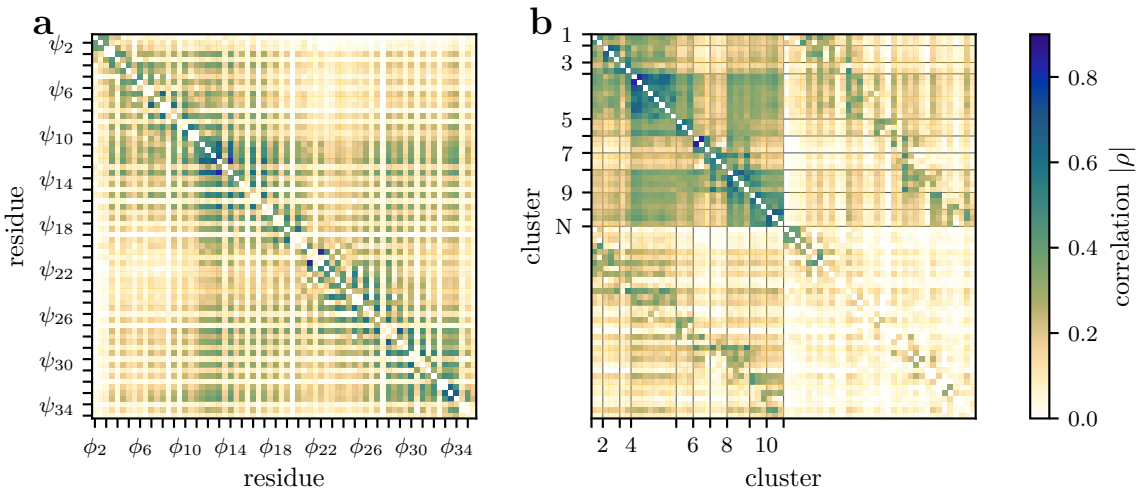

c

ϕ/ψ of the Leiden/CPM clusters

cluster 1 :	ϕ_4, ϕ_3
cluster 2 :	ψ_7, ψ_6, ψ_8
cluster 3 :	ϕ_{10}, ψ_9
cluster 4 :	$\psi_{12}, \psi_{13}, \phi_{12}, \psi_{16}, \psi_{15}, \psi_{11}, \phi_{11}, \psi_{14}$
cluster 5 :	$\psi_{18}, \psi_{19}, \psi_{17}$
cluster 6 :	$\psi_{21}, \psi_{20}, \phi_{22}$
cluster 7 :	$\psi_{24}, \psi_{22}, \psi_{23}$
cluster 8 :	$\psi_{27}, \psi_{26}, \psi_{28}, \psi_{25}$
cluster 9 :	$\psi_{29}, \psi_{30}, \psi_{31}$
cluster 10 :	$\phi_{33}, \psi_{33}, \psi_{32}$
noise N :	$\psi_1, \phi_2, \psi_2, \psi_3, \psi_4, \phi_5, \psi_5, \phi_6, \phi_7, \phi_8, \phi_9, \psi_{10}, \phi_{13}, \phi_{14}, \phi_{15}$
	$\phi_{16}, \phi_{17}, \phi_{18}, \phi_{19}, \phi_{20}, \phi_{21}, \phi_{23}, \phi_{24}, \phi_{25}, \phi_{26}, \phi_{27}, \phi_{28}, \phi_{29}, \phi_{30}, \phi_{31}$
	$\phi_{32}, \phi_{34}, \psi_{34}, \phi_{35}$

Figure S2: Preselection of backbone dihedral angles. For all dihedral angles the (a) pairwise correlations with all other dihedral angles, and the (b) corresponding Leiden/CPM clusters including (c) the tabular representation. The resolution parameter $\gamma = 0.45$ was optimized by silhouette score using cross validation, and all clusters containing only a single coordinate were sorted into the cluster *N*. Gaussian filtered angles with $\sigma = 2\,\mathrm{ns}$ were used.

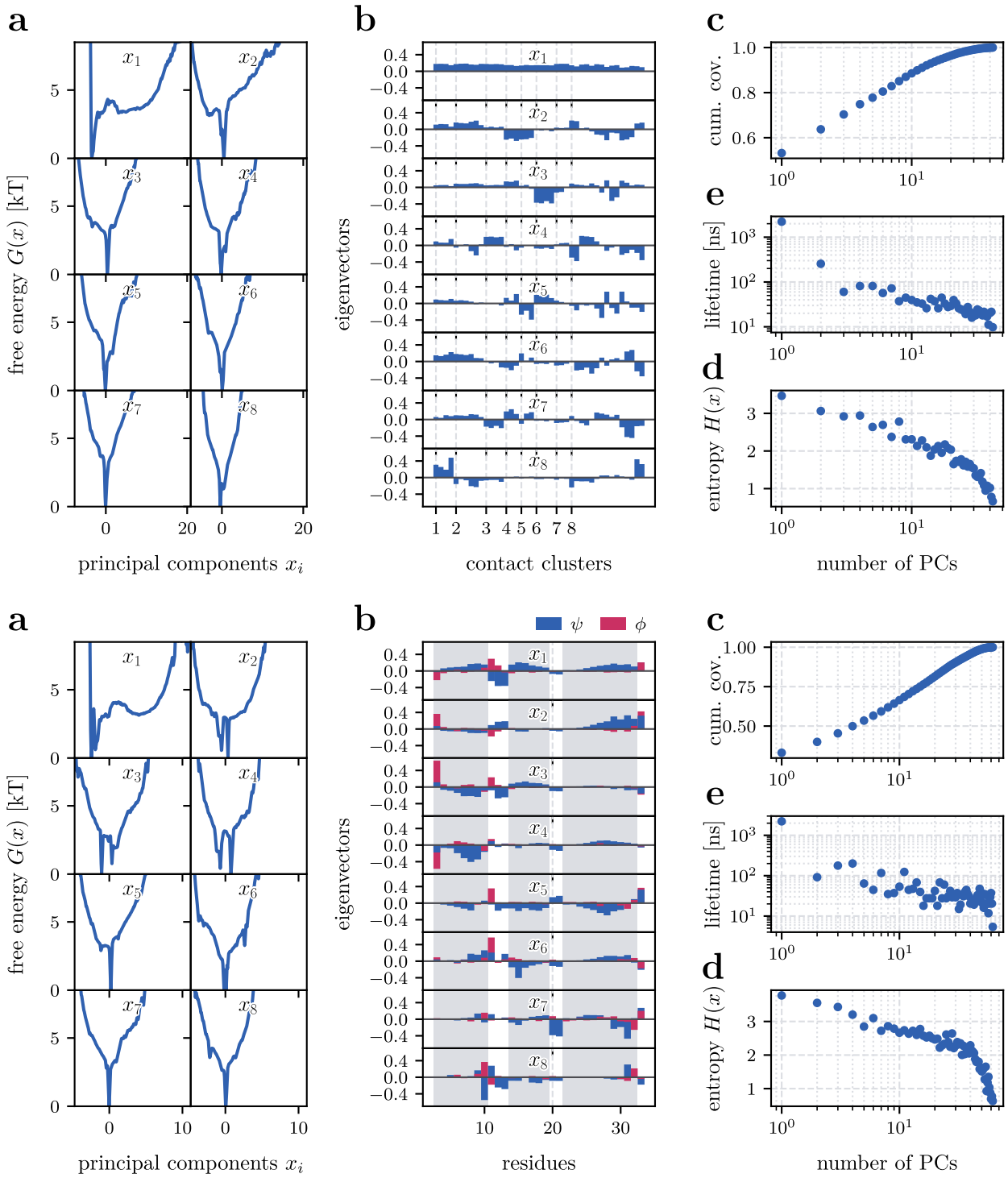

Figure S3: Selection of principal components x_i for (top) contact distances, and (bottom) backbone dihedral angles. (a) Free energy curves, (b) corresponding eigenvectors, (c) cumulative covariance of the first n principal components, and (d) lifetime $\tau : \mathrm{ACF}(\tau) = e^{-1}$ of the principal components. (d) Shannon entropy $H(X) = -\sum_{x \in X} p(x) \ln p(x)$, which provides an information theoretic approach to rank the principal components by their importance. This approach is based on the fact that entropy is a measure to measure the amount of information contained in a component.

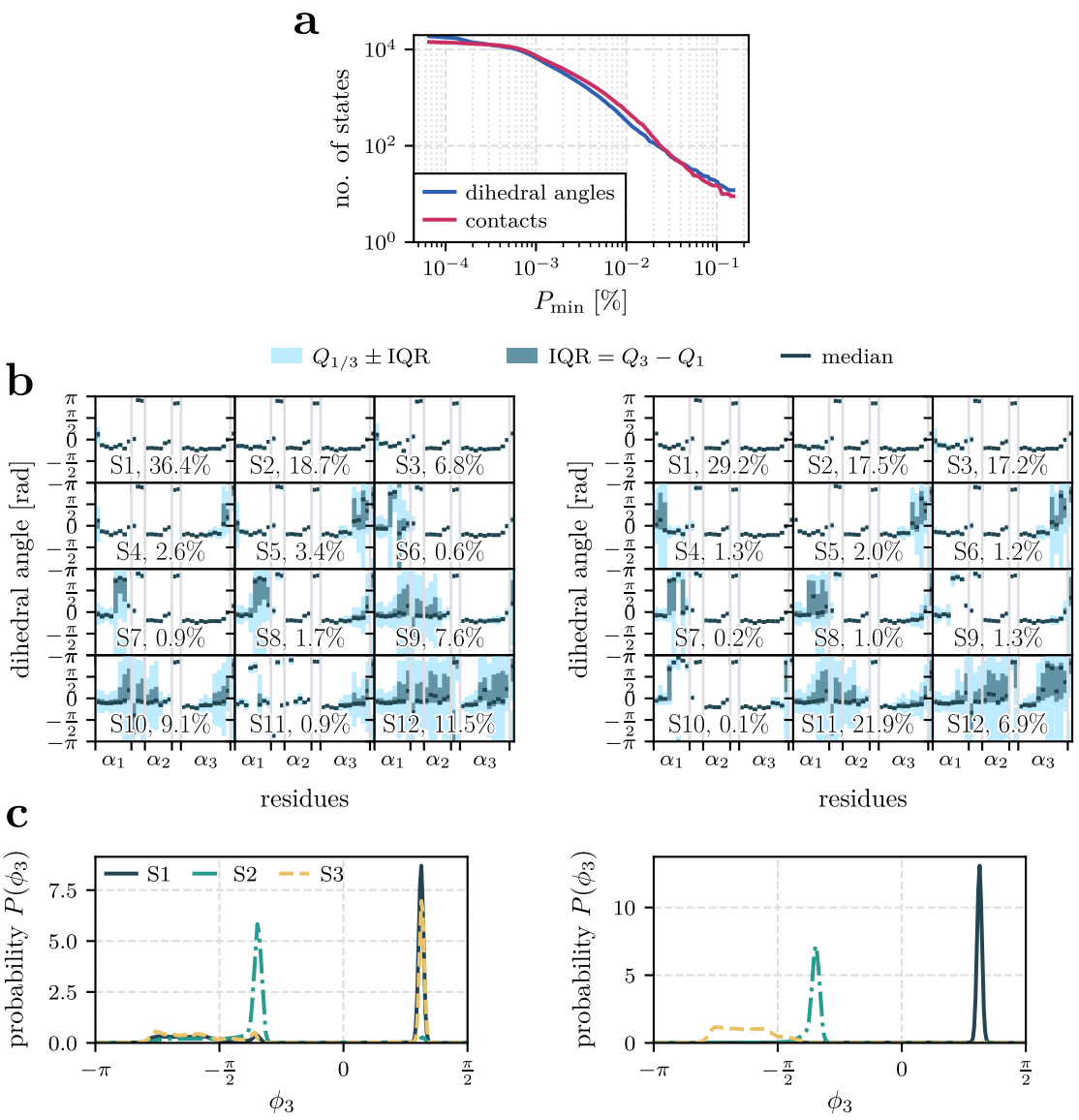

Figure S4: Further characterization of metastable states. (a) Resulting number of states for varying minimal population $P_{\min}$, used for the density-based clustering algorithm.[S3] (b) Structural characterization of the twelve metastable states of HP35, obtained for (left) contacts and (right) dihedral angles. The states are ordered by decreasing fraction of native contacts Q. As for most residues the ψ angles are more important than the corresponding ϕ (see Fig. S2), we restrict the representation to ψ angles only for the sake of clarity. Since the ψ angles exhibit a bimodal distribution (reflecting $\alpha \leftrightarrow \beta$) such that mean and variance do not well describe the data, we use a box-plot representation with quartiles Q_i (comprising the first $i \cdot 25\,\%$ of the data) that define the median Q_2, the interquartile range IQR $= Q_3 - Q_1$ and the lower (upper) bound as the smallest (largest) data point in $Q_{1/3} \pm$ IQR. (c) Comparing the ϕ_3 distribution of the 3 major natives states based on (left) contacts and (right) dihedral angles.

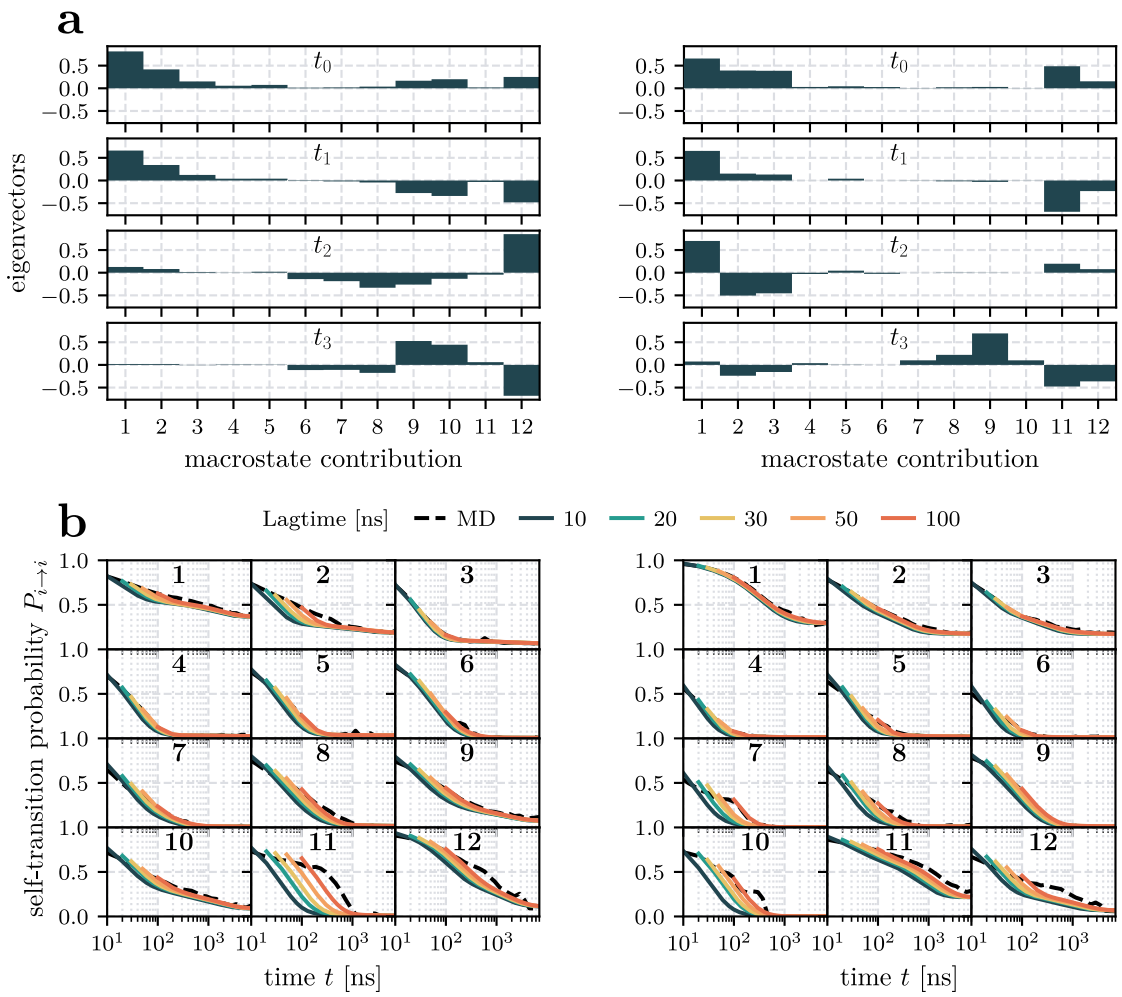

Figure S5: Further analysis and validation of the Markov state models, obtained by using the Hummer-Szabo projection.[S4] (a) Left eigenvector corresponding to the four slowest processes t_i of the twelve-state Markov model, obtained for (left) contacts and (right) dihedral angles, where t_0 corresponds to the stationary process and t_i with $i \geq 1$ to the i-th implied timescale. (b) Chapman-Kolmogorov tests of the twelve states for varying lag times, obtained for (left) contacts and (right) dihedral angles.

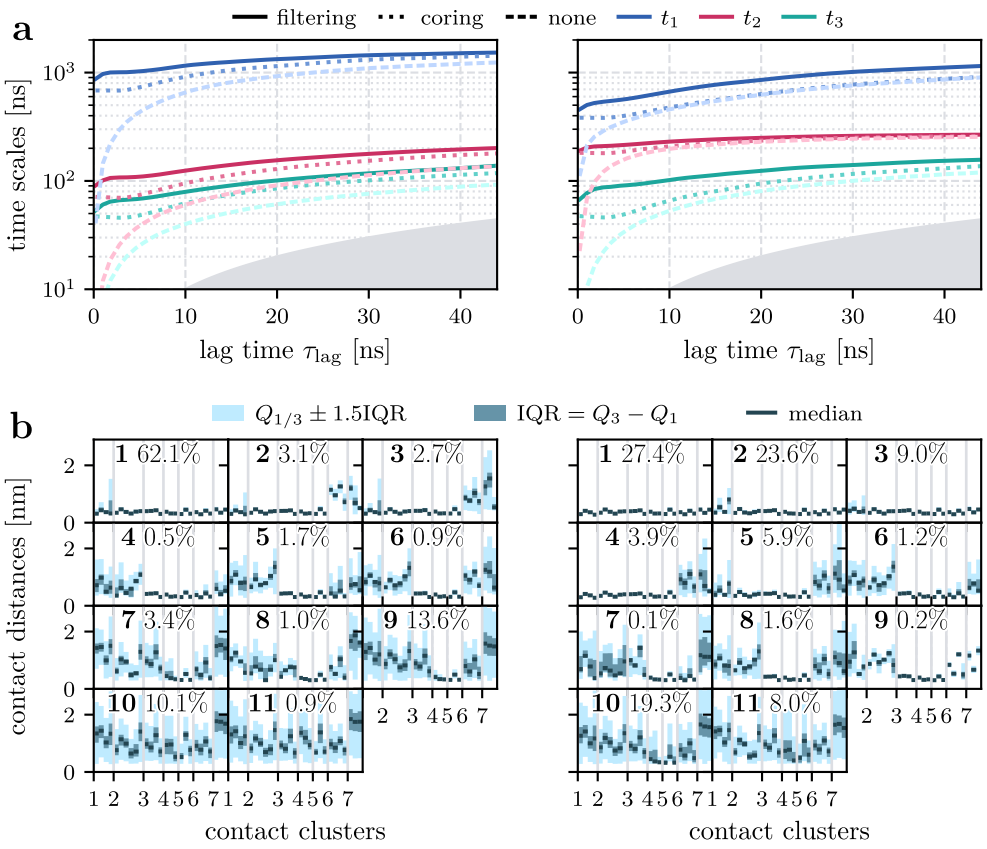

Figure S6: Effects of Gaussian filtering of the feature trajectory, compared to dynamic coring[S5] and using no dynamical correction. To this end, we repeated the MSM workflow described in the main paper (PCA, density-based clustering, and MPP), using the same parameters except for a lower minimum population of $P_{\mathrm{min}} = 15$, which ensures a comparable number of microstates when no dynamical correction is employed. In the case of dynamic coring, we used the previously determined[S5,S6] coring time $\tau_{\mathrm{cor}} = 3\,\mathrm{ns}$, which is expected to result in a similar effect as the Gaussian filtering with $\sigma = 2\,\mathrm{ns}$. (a) Three slowest implied timescales t_i of the various MSMs, obtained via the Hummer-Szabo projection[S4] for (left) contacts and (right) dihedral angles. (b) Structural characterization of the associated eleven metastable states obtained for dynamical coring. As in the main paper, the states are ordered by decreasing fraction of native contacts Q, and the contacts are ordered according to the seven main MoSAIC clusters (Fig. 5). For each state, the distribution of contact distances are represented by the median Q_2, the interquartile range $\mathrm{IQR} = Q_3 - Q_1$ and the lower (upper) bound as the smallest (largest) data point in $Q_{1/3} \pm 1.5\,\mathrm{IQR}$.

Table S2: Timescales $t_{ij} = R_{ij}^{-1}$ (in units of ns) obtained from the transition rate matrix $R \equiv I - T$, based on the transition matrix T obtained via the Hummer-Szabo projection[S4] and a lag time of $\tau_{\text{lag}} = 10\,\text{ns}$.

(a) contact-based states

state from	state to											
	1	2	3	4	5	6	7	8	9	10	11	12
1	**56**	85	282	874	899	22110	18335	124102	11918	65753	787242	–
2	43	**38**	389	2732	4439	348816	192317	–	12390	72459	–	130282
3	53	140	**37**	2170	2545	7932	13880	13296	22930	43798	160156	–
4	62	485	639	**35**	126	–	–	3311	7380	1376	–	–
5	85	622	1447	173	**44**	53415	–	2661	8030	848	32664	1144
6	298	–	720	19767	–	**58**	154	208	730	8194	21996	75361
7	481	1517	1483	–	–	238	**34**	62	164	86747	5105	–
8	1933	21837	8567	2792	2919	637	115	**50**	440	202	1004	8223
9	2446	4139	18826	15986	–	7113	1490	2440	**48**	60	1143	809
10	20124	151396	68743	5985	2214	19034	–	913	73	**43**	940	151
11	–	–	19678	67430	12493	4685	22802	517	141	83	**44**	666
12	–	24240	–	–	3525	–	–	–	1056	192	9301	**158**

(b) dihedral-based states

state from	state to											
	1	2	3	4	5	6	7	8	9	10	11	12
1	**275**	1326	890	21129	590	–	314425	36307	–	–	–	–
2	810	**49**	55	3199	45046	1341	807635	–	–	–	12612	–
3	517	54	**40**	495	8047	709	920568	4145	31999	551245	1261	75844
4	942	178	42	**25**	–	1038	1765	294	2022	–	180	–
5	41	–	715	–	**35**	742	–	7796	62859	881117	1420	4188
6	2390	96	50	6605	536	**24**	–	538	4561	49496	194	719
7	77350	1947	728	323	123737	–	**26**	134	41	–	329	–
8	5987	–	298	225	4127	488	378	**32**	118	2879	83	–
9	–	14948	2091	1728	–	7518	291	175	**54**	420	137	–
10	–	–	2192	–	221942	4125	–	369	49	**38**	241	–
11	34526	14370	1519	2937	14108	3661	33608	1676	2627	85643	**97**	128
12	–	–	–	–	43900	3610	–	–	–	–	41	**41**

Table S3: List of the main folding pathways assuming that we start in state 12 and end in state 1. Compared are (left) the paths found in the MD trajectory and (right) the most probable folding pathways identified by MSMPathfinder[S6] based on the transition matrix T obtained via the Hummer-Szabo projection[S4] with $\tau_{\text{lag}} = 10\,\text{ns}$.

(a) contacts-based states

MD Pathways	Freq	Length [µs]
(12, 10, 9, 1)	6	3.28
(12, 10, 5, 1)	6	2.41
(12, 10, 8, 1)	3	0.72
(12, 9, 10, 4, 1)	2	1.74
(12, 10, 9, 7, 1)	2	1.66
(12, 10, 1)	2	1.97
(12, 10, 9, 8, 1)	2	2.91
(12, 5, 1)	1	0.35
(12, 9, 10, 5, 4, 3, 1)	1	1.98
(12, 5, 2, 1)	1	0.05
(12, 9, 10, 1)	1	1.88
(12, 10, 7, 1)	1	9.85
(12, 10, 9, 8, 7, 1)	1	0.78
(12, 10, 8, 6, 1)	1	2.97
(12, 10, 8, 3, 1)	1	2.83
(12, 9, 8, 7, 1)	1	3.94
(12, 9, 10, 7, 8, 1)	1	1.85
(12, 10, 9, 8, 6, 1)	1	6.70
Tot. events	34	

MSM Pathways	Prob %	Length [µs]
(12, 10, 5, 1)	9.20	2.09
(12, 10, 9, 1)	8.77	2.14
(12, 10, 9, 2, 1)	8.01	2.21
(12, 5, 1)	7.52	1.94
(12, 10, 1)	4.10	2.09
(12, 10, 4, 1)	3.42	2.25
(12, 9, 1)	3.17	2.08
(12, 9, 2, 1)	2.95	2.36
(12, 10, 5, 4, 1)	2.06	2.21
(12, 10, 8, 1)	2.02	2.31
(12, 9, 10, 5, 1)	1.76	2.28
(12, 5, 4, 1)	1.46	2.04
(12, 10, 5, 2, 1)	1.41	2.05
(12, 10, 8, 7, 1)	1.39	2.08
(12, 10, 9, 4, 1)	1.34	2.21
(12, 5, 2, 1)	1.21	2.13
(12, 10, 8, 6, 1)	1.15	2.18
(12, 10, 9, 7, 1)	1.09	2.52
Tot. probability	62.03 %	

(b) dihedrals-based states

MD Pathways	Freq	Length [µs]
(12, 11, 3, 2, 1)	5	5.57
(12, 11, 4, 3, 2, 1)	5	3.23
(12, 11, 1)	4	2.18
(12, 11, 6, 2, 1)	2	0.92
(12, 11, 2, 1)	2	5.11
(12, 11, 3, 2, 4, 1)	1	0.38
(12, 11, 8, 3, 2, 1)	1	1.19
(12, 11, 8, 3, 6, 2, 5, 1)	1	4.33
(12, 11, 3, 6, 5, 1)	1	1.88
(12, 11, 8, 5, 1)	1	2.57
(12, 11, 2, 5, 1)	1	3.71
(12, 6, 2, 1)	1	0.43
(12, 11, 9, 8, 3, 2, 1)	1	5.15
(12, 11, 6, 5, 1)	1	4.68
(12, 11, 5, 1)	1	11.67
Tot. events	28	

MSM Pathways	Prob %	Length [µs]
(12, 11, 3, 1)	21.77	2.36
(12, 11, 3, 2, 1)	10.10	2.38
(12, 11, 4, 3, 1)	6.42	2.40
(12, 11, 5, 1)	5.84	2.01
(12, 11, 2, 3, 1)	4.69	2.45
(12, 11, 1)	4.50	1.93
(12, 11, 6, 3, 1)	4.33	2.43
(12, 11, 2, 1)	3.21	2.37
(12, 11, 4, 3, 2, 1)	3.02	2.53
(12, 11, 8, 3, 1)	2.85	2.39
(12, 11, 6, 3, 2, 1)	2.14	2.53
(12, 11, 6, 2, 3, 1)	2.03	2.60
(12, 11, 4, 2, 3, 1)	1.88	2.37
(12, 11, 8, 4, 3, 1)	1.63	2.38
(12, 11, 4, 2, 1)	1.40	2.35
Tot. probability	75.82 %	

References

(S1) Kubelka, J.; Chiu, T. K.; Davies, D. R. et al. Sub-microsecond protein folding. *J. Mol. Biol.* **2006**, *359*, 546–553.

(S2) Piana, S.; Lindorff-Larsen, K.; Shaw, D. E. Protein folding kinetics and thermodynamics from atomistic simulation. *Proc. Natl. Acad. Sci. USA* **2012**, *109*, 17845–17850.

(S3) Sittel, F.; Stock, G. Robust Density-Based Clustering to Identify Metastable Conformational States of Proteins. *J. Chem. Theory Comput.* **2016**, *12*, 2426–2435.

(S4) Hummer, G.; Szabo, A. Optimal Dimensionality Reduction of Multistate Kinetic and Markov-State Models. *J. Phys. Chem. B* **2015**, *119*, 9029–9037.

(S5) Nagel, D.; Weber, A.; Lickert, B. et al. Dynamical coring of Markov state models. *J. Chem. Phys.* **2019**, *150*, 094111.

(S6) Nagel, D.; Weber, A.; Stock, G. MSMPathfinder: Identification of pathways in Markov state models. *J. Chem. Theory Comput.* **2020**, *16*, 7874 – 7882.